A Kinetics Approach to Surface Wrinkling of Elastic Thin Films

Rui Huang

Department of Aerospace Engineering and Engineering Mechanics, University of Texas at Austin, Austin, TX 78712

Complex wrinkle patterns have been observed in various thin film systems, typically with integrated hard and soft materials for various applications as well as in nature. The underlying mechanism of wrinkling has been generally understood as a stress-driven instability. On an elastic substrate, equilibrium and energetics set the critical condition and select the wrinkle wavelength and amplitude. On a viscous substrate, wrinkles grow over time and kinetics select the fastest growing mode. Moreover, on a viscoelastic substrate, both energetics and kinetics play important roles in determining the critical condition, the growth rate, and wrinkle patterns. The dynamics of wrinkling, while analogous to other phase ordering phenomena, is rich and distinct under the effects of stress and film-substrate interactions. In this chapter, a kinetics approach is presented for wrinkling of isotropic and anisotropic elastic films on viscoelastic substrates. Analytic solutions are obtained by a linear perturbation analysis and a nonlinear energy minimization method, which predict the kinetics of wrinkle growth at the early stage and the equilibrium states at the long-time limit, respectively. In between, a power-law coarsening of the wrinkle wavelength is predicted by a scaling analysis. Furthermore, the kinetics approach enables numerical simulations that demonstrate emergence and transition of diverse wrinkle patterns (ordered and disordered) under various conditions.

1. Introduction

Theoretical studies of surface wrinkling may be traced back to 1940s when wrinkling of face struts was analyzed as a form of local elastic instability in structural sandwich panels [1-3]; an account of the historical development was well documented by Allen [4]. A series of works by Biot extended the wrinkling theory to viscoelastic layers [5] and rubber-like nonlinear elastic media under finite strain [6]. The early studies of wrinkling focused on the critical conditions for onset of instability as a failure mechanism for layered structures. Recent advances in micro/nanoscale fabrication and measurements have renewed the interest in mechanics of

wrinkling. In particular, wrinkling has also been exploited as an enabling mechanism for a variety of applications, such as stretchable electronics [7-9], micro/nano-fabrication [10-12], optical phase grating [13], smart adhesion [14], and metrology aid for measuring mechanical properties of thin films [15-17].

Wrinkling often occurs when a stiff surface layer on a drastically more compliant substrate is subject to compression in a direction parallel to the surface. Many approaches may induce compression and wrinkling. Mechanically, the surface layer can be put under compression by directly compressing the substrate or by bending the substrate. Interestingly, stretching the substrate could also induce compression in the surface layer [18], due to Poisson's effect. Typically the substrate (e.g., elastomer) has a larger Poisson's ratio than the surface layer (e.g., metal), and the mismatch induces compression of the surface layer in the direction perpendicular to the direction of stretch. More effectively, by attaching the surface layer to a pre-stretched substrate, the surface layer is compressed upon releasing the pre-stretch and the resulting wrinkles are stable without the need to apply external forces. Moreover, many non-mechanical approaches have also been reported to cause wrinkling, which often relies on a particular physical mechanism to induce an eigenstrain in the surface layer. A common approach of this kind is thermally induced wrinkling [10, 17, 19, 20], with the eigenstrain resulting from differential thermal expansion among the layers. A similar mechanism in biological systems is differential tissue growth in skin layers [21, 22] and human brain [23]. Other mechanisms include absorption-induced swelling [24] and phase transition [25]. In general, one may assume a residual stress in the surface layer as the driving force for wrinkling, regardless of the physical origin.

Notably, surface wrinkling may occur without any surface layer [26-28]. As predicted by Biot [6], the surface of a homogeneous block of rubber-like material becomes unstable under compression beyond a moderately large strain. Similar surface instability has been predicted for swollen hydrogels [29]. This type of surface instability, however, requires a nonlinear constitutive behavior of the material and is not addressed here.

In this chapter, we focus on a model system as shown in Fig. 1: an elastic film of thickness h lying on a viscoelastic layer of thickness H, which in turns lies on a rigid foundation. At the reference state (Fig. 1a), both layers are flat and the elastic film is subjected to a uniformly distributed residual stress, while the viscoelastic layer is stress free. A Cartesian coordinate

system is set up such that the $x-y$ plane coincides with the interface between the two layers. Figure 1(b) sketches a wrinkled state, where the elastic film undergoes a buckling deformation while the viscoelastic layer deforms concomitantly. The interface is assumed to be perfectly bonded at the wrinkled state.
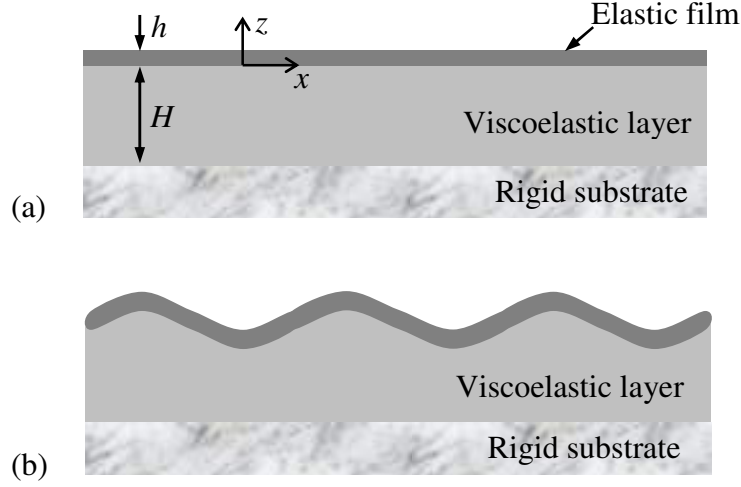

Figure 1. Schematic of an elastic film on a viscoelastic substrate: (a) the reference state, and (b) a wrinkled state.

Consideration of a viscoelastic layer underneath an elastic film leads to a kinetics approach to wrinkling [30-34]. Alternatively, an energy-based statics approach has been widely adopted for post-instability analysis to determine the equilibrium states of wrinkling for an elastic film on an elastic substrate [35-40]. Compared to the static equilibrium approach, which typically presumes specific wrinkle patterns, the kinetics approach offers a physical pathway to a variety of ordered and disordered wrinkle patterns without *a priori* assumptions. A similar kinetics approach has also been developed for wrinkling of an elastic film on a viscous substrate [41-44].

2. Deformation and equilibrium of an elastic film

Consider a cubic crystal film with the surface normal in the [001] direction. For convenience, the x and y axes are set to align with the [100] and [010] directions of the crystal at the reference state. The residual stress in the film generally have three in-plane components, σ_{xx}^R

3

, σ_{yy}^R, and σ_{xy}^R, as illustrated in Figure 2 (a). The stress state can also be represented by two principal stresses (σ_1 and σ_2) and the corresponding principal angle (θ_p), as illustrated in Figure 2 (b). As a necessary condition for the film to wrinkle, at least one of the two principal stresses must be negative (compressive). The resulting wrinkle pattern depends on the ratio between the two principal stresses for an isotropic film. For an anisotropic crystal film, the wrinkle pattern also depends on the principal direction of the residual stress [33].
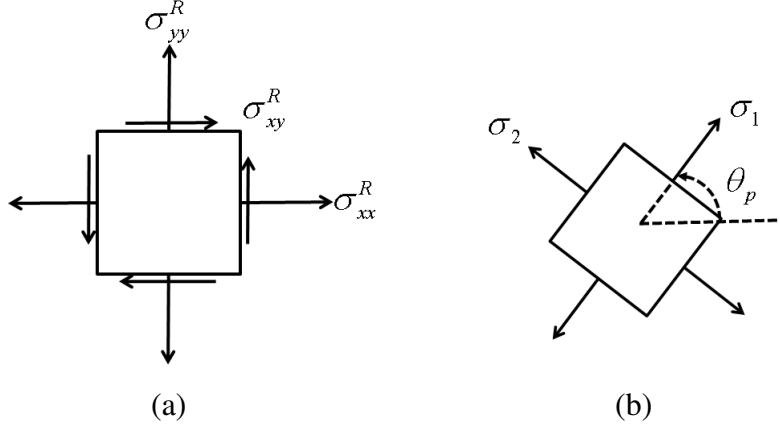

(a)   (b)

Figure 2. Residual stress in a film represented by stress elements: (a) in the x-y coordinates; (b) in the principal directions.

Let u_x and u_y be the in-plane displacements and w the out-of-plane deflection of the film. Upon wrinkling, the membrane strain components in the film are

$$\varepsilon_{xx} = \frac{\partial u_x}{\partial x} + \frac{1}{2}\left(\frac{\partial w}{\partial x}\right)^2, \tag{1}$$

$$\varepsilon_{yy} = \frac{\partial u_y}{\partial y} + \frac{1}{2}\left(\frac{\partial w}{\partial y}\right)^2, \tag{2}$$

$$\varepsilon_{xy} = \frac{1}{2}\left(\frac{\partial u_x}{\partial y} + \frac{\partial u_y}{\partial x}\right) + \frac{1}{2}\frac{\partial w}{\partial x}\frac{\partial w}{\partial y}. \tag{3}$$

A nonlinear term is included above in each strain component to account for geometrical nonlinearity due to moderately large deflection of the elastic film [45, 46]. It shall be noted that the displacements are measured relative to the reference state with the residual stress $\sigma_{\alpha\beta}^R$, and

thus the strains in Eqs. (1)-(3) describe an incremental deformation from the stressed reference state.

The membrane forces in the film, including the initial residual stresses, are

$$N_{\alpha\beta} = \left(\sigma_{\alpha\beta}^R + \sigma_{\alpha\beta}\right)h \ , \tag{4}$$

where the Greek subscripts (α, β) represent the in-plane coordinates x and y, and by linear elasticity

$$\begin{bmatrix} \sigma_{xx} \\ \sigma_{yy} \\ \sigma_{xy} \end{bmatrix} = \begin{bmatrix} \tilde{C}_{11} & \tilde{C}_{12} & 0 \\ \tilde{C}_{12} & \tilde{C}_{22} & 0 \\ 0 & 0 & 2C_{66} \end{bmatrix} \begin{bmatrix} \varepsilon_{xx} \\ \varepsilon_{yy} \\ \varepsilon_{xy} \end{bmatrix}. \tag{5}$$

For a cubic crystal film, the elastic moduli are: $\tilde{C}_{11} = \tilde{C}_{22} = C_{11} - C_{12}^2 / C_{11}$ and $\tilde{C}_{12} = C_{12} - C_{12}^2 / C_{11}$. For an isotropic elastic plate, the reduced elastic constants can be expressed in terms of Young's modulus (E) and Poisson's ratio (ν), namely, $\tilde{C}_{11} = \tilde{C}_{22} = E / (1 - \nu^2)$, $\tilde{C}_{12} = \nu E / (1 - \nu^2)$, and $C_{66} = E / [2(1 + \nu)]$.

The moment intensities are

$$\begin{bmatrix} M_{xx} \\ M_{yy} \\ M_{xy} \end{bmatrix} = \frac{h^3}{12} \begin{bmatrix} \tilde{C}_{11} & \tilde{C}_{12} & 0 \\ \tilde{C}_{12} & \tilde{C}_{22} & 0 \\ 0 & 0 & 2C_{66} \end{bmatrix} \begin{bmatrix} \kappa_{xx} \\ \kappa_{yy} \\ \kappa_{xy} \end{bmatrix}. \tag{6}$$

where $\kappa_{\alpha\beta} = \dfrac{\partial^2 w}{\partial x_\alpha \partial x_\beta}$ is the curvature tensor.

For the film to be in equilibrium at the wrinkled state, interfacial tractions are generally required in both the tangential and normal directions. First, in-plane force equilibrium requires that

$$\frac{\partial N_{xx}}{\partial x} + \frac{\partial N_{xy}}{\partial y} = T_x , \tag{7}$$

$$\frac{\partial N_{xy}}{\partial x} + \frac{\partial N_{yy}}{\partial y} = T_y , \tag{8}$$

where T_x and T_y are the shear tractions acting at the interface between the film and the substrate. In the normal direction, the force equilibrium requires that

$$\frac{\partial Q_x}{\partial x} + \frac{\partial Q_y}{\partial y} + \left[\frac{\partial}{\partial x}\left(N_{xx}\frac{\partial w}{\partial x} + N_{xy}\frac{\partial w}{\partial y} \right) + \frac{\partial}{\partial y}\left(N_{yy}\frac{\partial w}{\partial y} + N_{xy}\frac{\partial w}{\partial x} \right) \right] + p = 0, \quad (9)$$

where p is the pressure (negative normal traction) at the interface, Q_x and Q_y are the transverse shearing forces in the film. In addition, by the moment equilibrium, we have

$$\frac{\partial M_{xx}}{\partial x} + \frac{\partial M_{xy}}{\partial y} + Q_x = 0, \tag{10}$$

$$\frac{\partial M_{xy}}{\partial x} + \frac{\partial M_{yy}}{\partial y} + Q_y = 0. \tag{11}$$

With Eqs. (10) and (11), the shear forces in Eq. (9) can be eliminated, namely

$$\begin{aligned}
&\frac{\partial^2 M_{xx}}{\partial x^2} + 2\frac{\partial^2 M_{xy}}{\partial x \partial y} + \frac{\partial^2 M_{yy}}{\partial y^2} \\
&- \left[\frac{\partial}{\partial x}\left(N_{xx}\frac{\partial w}{\partial x} + N_{xy}\frac{\partial w}{\partial y} \right) + \frac{\partial}{\partial y}\left(N_{yy}\frac{\partial w}{\partial y} + N_{xy}\frac{\partial w}{\partial x} \right) \right] = p
\end{aligned} \tag{12}$$

Further by substituting Eq. (6) into (12), we obtain that

$$\begin{aligned}
&\frac{h^3}{12}\left[\tilde{C}_{11}\frac{\partial^4 w}{\partial x^4} + 2(\tilde{C}_{12} + 2C_{66})\frac{\partial^4 w}{\partial x^2 \partial y^2} + \tilde{C}_{22}\frac{\partial^4 w}{\partial y^4} \right] \\
&- \left[\frac{\partial}{\partial x}\left(N_{xx}\frac{\partial w}{\partial x} + N_{xy}\frac{\partial w}{\partial y} \right) + \frac{\partial}{\partial y}\left(N_{yy}\frac{\partial w}{\partial y} + N_{xy}\frac{\partial w}{\partial x} \right) \right] = p
\end{aligned} \tag{13}$$

For an isotopic elastic film, Eq. (13) reduces to

$$\begin{aligned}
&\frac{Eh^3}{12(1-v^2)}\left(\frac{\partial^4 w}{\partial x^4} + 2\frac{\partial^4 w}{\partial x^2 \partial y^2} + \frac{\partial^4 w}{\partial y^4} \right) \\
&- \left[\frac{\partial}{\partial x}\left(N_{xx}\frac{\partial w}{\partial x} + N_{xy}\frac{\partial w}{\partial y} \right) + \frac{\partial}{\partial y}\left(N_{yy}\frac{\partial w}{\partial y} + N_{xy}\frac{\partial w}{\partial x} \right) \right] = p
\end{aligned} \tag{14}$$

which is well known as the von-Karman plate equation [45, 46].

Therefore, the deformation of the elastic film is described by the displacements (u_x, u_y, w), the membrane strain ($\varepsilon_{\alpha\beta}$), and the curvature ($\kappa_{\alpha\beta}$). The constitutive relations in (4-6) give the membrane forces ($N_{\alpha\beta}$) and moments ($M_{\alpha\beta}$), assuming linear elasticity. The tractions (T_x, T_y, p) at the interface are then obtained from the equilibrium equations in (7), (8), and (12).

3. Kinetics: deformation of a viscoelastic layer

Subject to the interfacial tractions, the viscoelastic layer undergoes a time-dependent deformation. By the linear theory of viscoelasticity [47], the stress-strain relationship for the viscoelastic material takes an integral form

$$\sigma_{ij}(t) = 2\int_{-\infty}^{t} \mu(t-\tau)\frac{\partial \varepsilon_{ij}(\tau)}{\partial \tau}d\tau + \delta_{ij}\int_{-\infty}^{t} \lambda(t-\tau)\frac{\partial \varepsilon_{kk}(\tau)}{\partial \tau}d\tau, \tag{15}$$

where $\mu(t)$ and $\lambda(t)$ are the viscoelastic relaxation moduli, δ_{ij} is the Kronecker delta.

The Laplace transform of (15) is

$$\tilde{\sigma}_{ij}(s) = 2s\tilde{\mu}(s)\tilde{\varepsilon}_{ij}(s) + s\tilde{\lambda}_{ij}(s)\tilde{\varepsilon}_{kk}(s)\delta_{ij}, \tag{16}$$

where a tilt over a variable designates its Laplace transform with respect to time and s is the transform variable. The Laplace transformed stress-strain relation is identical to that of linear elasticity with the elastic moduli $s\tilde{\mu}(s)$ and $s\tilde{\lambda}(s)$. As a result, a viscoelasticity problem often can be solved by the method of Laplace transform based on the solution of a corresponding elasticity problem, referred to as the correspondence principle [47].

Consider a viscoelastic layer ($0 \geq z \geq -H$), which is stress free initially ($t=0$) and subjected to normal and shear tractions at the upper surface for $t>0$, namely

$$\sigma_{zz} = S_z(x,y,t) \text{ and } \sigma_{z\alpha} = S_\alpha(x,y,t) \text{ at } z=0. \tag{17}$$

The lower surface of the layer is bonded to a rigid substrate, where the displacement is zero:

$$u_\alpha = u_z = 0 \text{ at } z = -H. \tag{18}$$

Assume a plane-strain condition ($S_y = u_y = 0$) with periodic surface tractions in the form

$$S_x = A(t)\sin kx, \tag{19}$$

$$S_z = B(t)\cos kx, \tag{20}$$

where k is the wave number, $A(t)$ and $B(t)$ are time-dependent amplitudes.

By solving the corresponding elasticity problem [30], the Laplace transform of the displacements at the surface of the viscoelastic layer are obtained as

$$\tilde{u}_x^s(x,s) = \frac{1}{2ks\tilde{\mu}(s)}\left[\gamma_{11}(s\tilde{v},kH)\tilde{A}(s) + \gamma_{12}(s\tilde{v},kH)\tilde{B}(s)\right]\sin(kx), \tag{21}$$

$$\tilde{u}_z^s(x,s) = \frac{1}{2ks\tilde{\mu}(s)}\left[\gamma_{21}(s\tilde{v},kH)\tilde{A}(s) + \gamma_{22}(s\tilde{v},kH)\tilde{B}(s)\right]\cos(kx), \tag{22}$$

where

$$\gamma_{11} = \frac{1+\kappa}{4} \frac{\kappa \sinh(2kH) + 2kH}{\kappa \cosh^2(kH) + (kH)^2 + \left(\frac{1-\kappa}{2}\right)^2}, \tag{23}$$

$$\gamma_{22} = \frac{1+\kappa}{4} \frac{\kappa \sinh(2kH) - 2kH}{\kappa \cosh^2(kH) + (kH)^2 + \left(\frac{1-\kappa}{2}\right)^2}, \tag{24}$$

$$\gamma_{12} = \gamma_{21} = -\frac{\frac{\kappa(1-\kappa)}{2} \sinh^2(kH) + (kH)^2}{\kappa \cosh^2(kH) + (kH)^2 + \left(\frac{1-\kappa}{2}\right)^2}, \tag{25}$$

and $\kappa = 3 - 4s\tilde{v}(s)$ with $\tilde{v}(s) = \dfrac{\tilde{\lambda}(s)}{2s(\tilde{\mu}(s) + \tilde{\lambda}(s))}$ as Laplace transform of Poisson's ratio.

The solution in (21) and (22) indicates that, in general, the surface of the viscoelastic layer undergoes both out-of-plane and in-plane displacements. For a special case, when the layer is infinitely thick ($kH \rightarrow \infty$) and incompressible ($v = 0.5$), we have $\gamma_{12} = \gamma_{21} = 0$, and thus the two equations are decoupled:

$$\tilde{u}_x^s(x,s) = \frac{1}{4ks\tilde{\mu}(s)} \tilde{S}_x(x,s), \tag{26}$$

$$\tilde{u}_z^s(x,s) = \frac{1}{4ks\tilde{\mu}(s)} \tilde{S}_z(x,s). \tag{27}$$

Alternatively, if the viscoelastic layer is relatively thin ($kH \rightarrow 0$), by keeping only the leading terms of kH in an asymptotic analysis [31, 34], Eqs. (21) and (22) become

$$\tilde{u}_x^s(x,s) = \frac{1}{2ks\tilde{\mu}(s)} \left[2kH\tilde{A}(s) + \frac{1-4v}{2(1-v)}(kH)^2 \tilde{B}(s) \right] \sin(kx), \tag{28}$$

$$\tilde{u}_z^s(x,s) = \frac{1}{2ks\tilde{\mu}(s)} \left[\frac{1-2v}{1-v}(kH)\tilde{B}(s) + \frac{1-4v}{2(1-v)}(kH)^2 \tilde{A}(s) \right] \cos(kx). \tag{29}$$

Here, the Poisson's ratio has been assumed to be a constant independent of time and $v < 0.5 - \frac{1}{6}(kH)^2$. On the other hand, when the Poisson's ratio approaches 0.5, the viscoelastic layer is nearly incompressible and Eq. (29) is replaced by

$$\tilde{u}_z^s(x,s) = \frac{1}{2ks\tilde{\mu}(s)} \left[\frac{2}{3}(kH)^3 \tilde{B}(s) - (kH)^2 \tilde{A}(s) \right] \cos(kx), \tag{30}$$

where the first term in the bracket scales with $(kH)^3$ instead of (kH) in Eq. (29). This leads to different kinetics of wrinkling for compressible and incompressible viscoelastic layers [32].
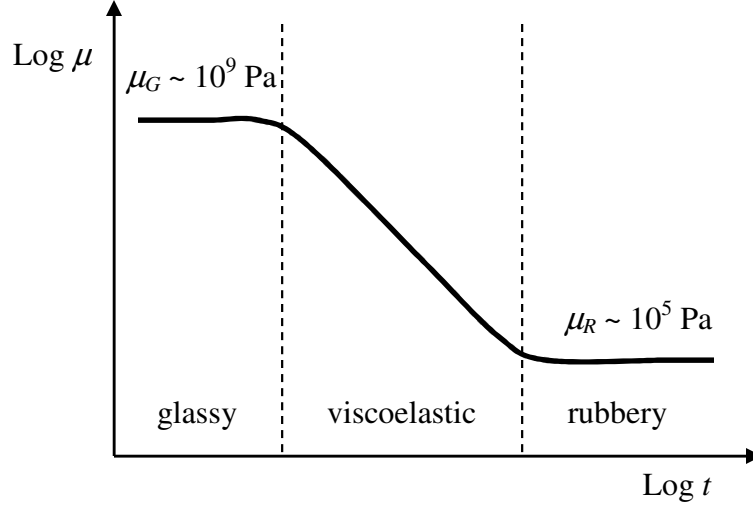
8

Figure 3. A schematic of the relaxation modulus as a function of time for a viscoelastic material.

Figure 3 depicts the relaxation shear modulus, $\mu(t)$, as a function of time for a typical cross-linked polymer, with the glassy modulus $\mu(0) = \mu_G$ at the short-time limit and the rubbery modulus $\mu(\infty) = \mu_R$ at the long-time limit. The modulus typically varies by several orders of magnitude: $\mu_0 \sim 10^9$ Pa and $\mu_\infty \sim 10^5$ Pa. In general, the Poisson's ratio is also a function of time, but the time dependence is much weaker. Experimentally measured relaxation modulus $\mu(t)$ is often interpreted in terms of a mechanical model consisting of an array of spring-dashpot analogs in parallel (Figure 4). To ensure a rubbery elastic limit at the long-time limit, one of the parallel branches must be a spring of modulus μ_R, with no dashpot. Each of the other parallel branches comprises a spring of modulus μ_i and a dashpot of viscosity η_i. With such a model, the relaxation modulus is

$$\mu(t) = \mu_R + \sum_i \mu_i \exp(-p_i t), \tag{31}$$

where $p_i = \mu_i / \eta_i$ is the relaxation parameter of one branch. The Laplace transform of the relaxation modulus is

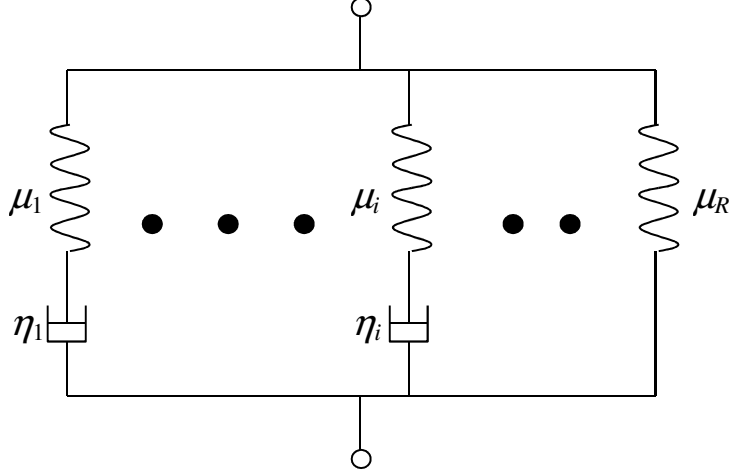$$\tilde{\mu}(s) = \frac{\mu_R}{s} + \sum_i \frac{\mu_i}{s + p_i}. \tag{32}$$

Figure 4. A mechanical analog model of a viscoelastic material.

For simplicity, consider the Kelvin model of linear viscoelasticity, modeled by a simple mechanical analog consisting of an elastic spring and a viscous dashpot in parallel, for which the Laplace transform of the relaxation modulus is

$$\tilde{\mu}(s) = \frac{\mu_R}{s} + \eta. \tag{33}$$

After substituting (33) into Eqs. (28) and (29), inverse Laplace transform leads to

$$\frac{\partial u_x^s}{\partial t} = \frac{H}{\eta} S_x + \frac{1-4\nu}{4(1-\nu)} \frac{H^2}{\eta} \frac{\partial S_z}{\partial x} - \frac{\mu_R}{\eta} u_x^s, \tag{34}$$

$$\frac{\partial u_z^s}{\partial t} = \frac{1-2\nu}{2(1-\nu)} \frac{H}{\eta} S_z - \frac{1-4\nu}{4(1-\nu)} \frac{H^2}{\eta} \frac{\partial S_x}{\partial x} - \frac{\mu_R}{\eta} u_z^s. \tag{35}$$

By dropping the H^2 terms under the thin-layer approximation ($kH \ll 1$), Eqs. (34) and (35) become

$$\frac{\partial u_x^s}{\partial t} = \frac{H}{\eta} S_x - \frac{\mu_R}{\eta} u_x^s, \tag{36}$$

$$\frac{\partial u_z^s}{\partial t} = \frac{1-2\nu}{2(1-\nu)} \frac{H}{\eta} S_z - \frac{\mu_R}{\eta} u_z^s. \tag{37}$$

Equation (36) is equivalent to a shear-lag model [48-50], which assumes a uniform shear stress across the thin layer. Equation (37) is similar to the Winkler model for an elastic foundation [4], but includes a time-dependent term accounting for the viscous effect. The two equations are uncoupled under the thin-layer approximation.

10

In the above development, plane-strain deformation and periodic surface tractions have been assumed. The restriction of periodic tractions has been relaxed by absorbing the wave number through a differentiation with respect to x in the course of the inverse Laplace transform. The resulting equations are independent of wave number and can thus be used for arbitrary tractions. At the end, the in-plane and out-of-plane responses are decoupled by the thin-layer approximation. Therefore, the restriction of plane-strain deformation can also be relaxed by generalizing the in-plane response, Eq. (36), for both x and y directions, namely

$$\frac{\partial u_\alpha^s}{\partial t} = \frac{H}{\eta} S_\alpha - \frac{\mu_R}{\eta} u_\alpha^s,$$ (38)

for $\alpha = x$ and y. Equations (37) and (38) then represent an approximate solution for the three-dimensional response of a thin viscoelastic layer subjected to the boundary conditions in (17) and (18). Following similar steps, other forms of viscoelastic solutions may be developed for incompressible and thick layers.

4. Evolution equations of wrinkling

By assuming the interface between the elastic film and the viscoelastic layer to remain bonded during wrinkling, the displacements and tractions are continuous across the interface, namely

$$S_z = -p, \; S_\alpha = T_\alpha,$$ (39)

$$u_z^s = w, \; u_\alpha^s = u_\alpha.$$ (40)

The time-dependent response of the viscoelastic layer can then be written in terms of the film displacements as

$$\frac{\partial w}{\partial t} = \frac{1-2\nu}{2(1-\nu)} \frac{H}{\eta}(-p) - \frac{\mu_R}{\eta} w,$$ (41)

$$\frac{\partial u_\alpha}{\partial t} = \frac{H}{\eta} T_\alpha - \frac{\mu_R}{\eta} u_\alpha,$$ (42)

where p and T_α are related to the displacements (w and u_α) by Eqs. (7), (8) and (12). Together with the constitutive relations of the film in Eqs. (4)-(6), we have a complete set of evolution equations for wrinkling.

Here, it is assumed that the evolution process is sufficiently slow such that inertia effects are negligible and the elastic film remains in equilibrium during evolution. Despite the

11

limitations in the simple viscoelastic property and the thin-layer approximation, the present model has been shown to be able to capture essential features of viscoelastic wrinkle evolution, such as the kinetics of wrinkle growth at the early stage and the equilibrium states at the long-time limit. Extension to more general cases is possible. Notably, Biot [5] developed a general instability theory for a viscoelastic layer on a semi-infinite viscoelastic substrate or embedded in an infinite viscoelastic medium, which may be extended to three-dimensional post-instability analysis. Alternatively, a Fourier transform method similar to that by Huang et al. [37] may be employed for an elastic film on an infinitely thick viscoelastic substrate. By combining Reynolds' lubrication theory with the nonlinear plate equations, Huang and Suo [42] developed a set of evolution equations for wrinkling of an elastic film on an incompressible viscous layer.

5. Initial growth

Start from a nearly flat film. At the early stage of wrinkling, the residual stress in the film is hardly relaxed, and the growth of wrinkles is predominantly due to out-of-plane displacement, uncoupled from the in-plane displacements. Substituting (14) into (41) for an isotropic film, we obtain that

$$\frac{\partial w}{\partial t} = -K w_{,\alpha\alpha\beta\beta} + F\left(N_{\alpha\beta} w_{,\beta}\right)_{,\alpha} - Rw, \tag{43}$$

where

$$K = \frac{(1-2\nu_s)E_f h^3 H}{24(1-\nu_s)(1-\nu_f^2)\eta_s}, \qquad F = \frac{1-2\nu_s}{2(1-\nu_s)}\frac{H}{\eta_s}, \qquad R = \frac{\mu_R}{\eta_s}. \tag{44}$$

Consider an equi-biaxial residual stress such that $N_{\alpha\beta} \approx -\sigma_0 h \delta_{\alpha\beta}$ ($\sigma_0 > 0$) at the early stage. The first two terms at the right-hand side of Eq. (43) compete to set a length scale

$$L_1 = \sqrt{\frac{K}{F\sigma_0 h}} = \sqrt{\frac{E_f h^2}{12(1-\nu_f^2)\sigma_0}}, \tag{45}$$

and a corresponding time scale

$$\tau_1 = \frac{K}{(F\sigma_0 h)^2} = \frac{(1-\nu_s)E_f \eta_s h}{6(1-2\nu_s)(1-\nu_f^2)\sigma_0^2 H}. \tag{46}$$

Neglecting the third term at the right-hand side of Eq. (43) for the moment, a linear perturbation analysis [31] leads to a critical wavelength,

$$\lambda_c = 2\pi L_1, \tag{47}$$

and the fastest growing wavelength,

$$\lambda_m = 2\sqrt{2}\pi L_1, \tag{48}$$

both proportional to the length scale, which in turn is proportional to the film thickness. The film is unstable for wrinkles with wavelengths $\lambda > \lambda_c$, and the wrinkle amplitude grows exponentially with time. The growth rate, inversely proportional to the time scale τ_1, peaks at the wavelength $\lambda = \lambda_m$, for which the wrinkle amplitude is given by

$$A = A_0 \exp\left(\frac{t}{4\tau_1}\right), \tag{49}$$

and A_0 is a constant for the initial amplitude. Therefore, at the early stage, the fastest growing mode dominates, with both the wrinkle wavelength and the growth rate depending on the residual stress via the length and time scales.

The third term at the right-hand side of Eq. (43) accounts for the effect of substrate elasticity, which does not change the fastest growing wrinkle wavelength but reduces the growth rate [31]. The substrate elasticity completely suppresses the wrinkling instability when the compressive residual stress is lower than a critical value. By setting the peak growth rate to be zero, one obtains the critical stress:

$$\sigma_c = \sqrt{\frac{4KR}{F^2 h^2}} = \sqrt{\frac{2(1-\nu_s)E_f \mu_R}{3(1-2\nu_s)(1-\nu_f^2)} \frac{h}{H}}. \tag{50}$$

Note that the critical stress in (50) decreases as the thickness ratio H/h increases, but this is only true for a relatively thin viscoelastic layer. For a thick substrate layer, the critical stress approaches a constant independent of the thickness ratio [30, 37].

For an anisotropic elastic film, a linear perturbation analysis predicts anisotropic wrinkle patterns at the early stage [33]. Consider a periodic wrinkle pattern, with a wave number k and an angle of the wave vector θ, namely

$$w(x, y, t) = A(t)\cos[k(x\cos\theta + y\sin\theta)]. \tag{51}$$

Here, the angle θ is measured from the x-axis or the [100] axis for the cubic crystal film. The wrinkle amplitude grows exponentially with time as

$$A(t) = A_0 \exp\left(\frac{\alpha_\theta t}{\tau}\right),$$

(52)

where $\tau = \eta_s / C_{11}$ is a time scale, and

$$\alpha_\theta = \frac{(1-2v_s)H}{24(1-v_s)C_{11}h}\left[-\overline{E}_\theta (kh)^4 - 12\sigma_\theta (kh)^2\right] - \frac{\mu_R}{C_{11}}.$$

(53)

The dimensionless growth rate in (53) depends on the angle θ through two quantities:

$$\sigma_\theta = \sigma_1\left[1 - \left(1 - \frac{\sigma_2}{\sigma_1}\right)\sin^2(\theta - \theta_p)\right],$$

(54)

$$\overline{E}_\theta = C_{11}\left[1 - \left(\frac{C_{12}}{C_{11}}\right)^2\right]\left[1 + \frac{(\xi - 1)C_{11}}{2(C_{11} + C_{12})}\sin^2 2\theta\right].$$

(55)

First, the ratio between the two principal stresses represents the stress anisotropy that determines the angular dependence of σ_θ. Hence an equi-bixial stress ($\sigma_2 / \sigma_1 = 1$) is isotropic. Second, $\xi = 2C_{66} / (C_{11} - C_{12})$ defines a degree of elastic anisotropy of the crystal. For an isotropic material, $\xi = 1$ and $\overline{E}_\theta$ reduces to $\overline{E}_f = E_f / (1 - v_f^2)$, independent of the angle.

Figure 5 compares the spectra of the initial wrinkle growth rate for both isotropic and anisotropic elastic films under various residual stresses [33]. Contours of the normalized growth rate α_θ are plotted in the plane spanning the x and y components of the wave vector, $k_x = k\cos\theta$ and $k_y = k\sin\theta$, both normalized by the film thickness h; only positive growth rates are plotted. In all the calculations, we set $\mu_R / C_{11} = 10^{-5}$, $H/h = 10$, and $v_s = 0.45$. The major principal stress $\sigma_1 / C_{11} = -0.003$ is fixed, while the ratio σ_2 / σ_1 is varied from 1 for equi-biaxial to 0 for uniaxial stress state. For the isotropic film, the growth spectrum is solely controlled by the stress ratio. Under an equi-biaxial residual stress ($\sigma_2 / \sigma_1 = 1$), the growth spectrum is isotropic with concentric circular contours and thus no favored directions. When the two principal stresses differ, the rotational symmetry is broken and the growth rate peaks at a particular wave vector in the direction of the major principal stress. Therefore, the kinetically dominant wrinkle pattern at the initial stage changes from non-directional (e.g., labyrinth pattern) to uni-directional (e.g., parallel striped pattern).
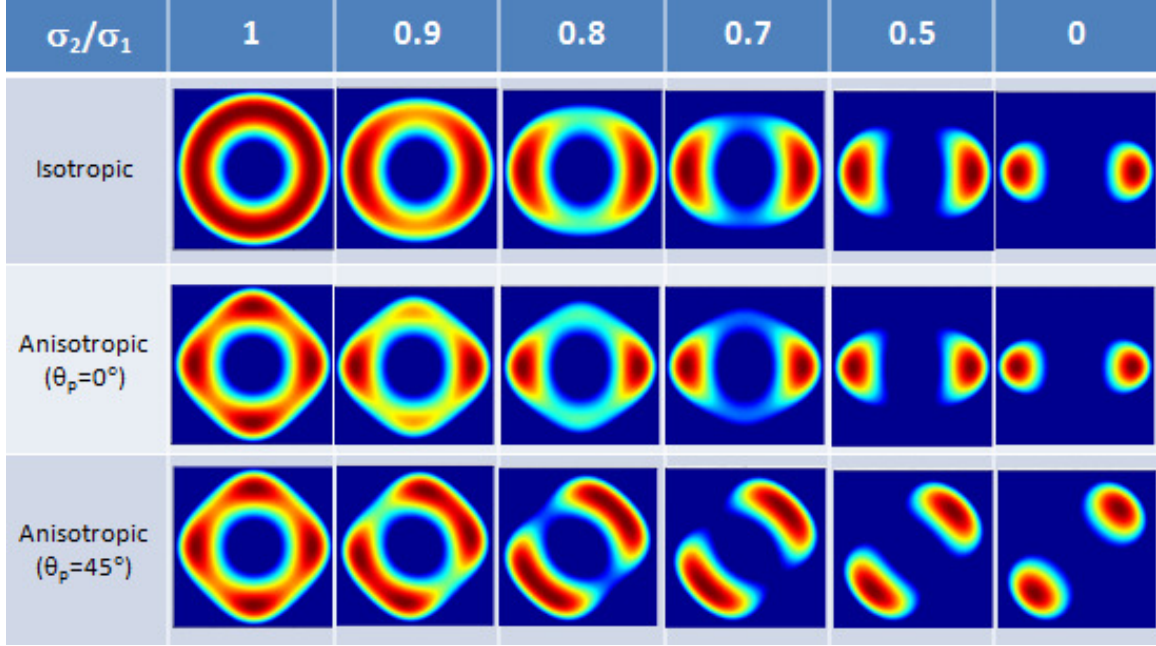
14

σ_2/σ_1	1	0.9	0.8	0.7	0.5	0
Isotropic						
Anisotropic ($\theta_p=0°$)						
Anisotropic ($\theta_p=45°$)						

Figure 5. Spectra of the wrinkle growth rate at the early stage for isotropic and anisotropic elastic films under various residual stress states. The major principal stress is $\sigma_1/C_{11} = -0.003$.

For a cubic crystal film (e.g., SiGe), the growth spectrum not only depends on the ratio between the two principal stresses but also depends on the direction of the principal stress (θ_p). Even under an isotropic equi-biaxial stress, an anisotropic growth spectrum emerges, with four peaks aligned in the two orthogonal crystal directions, [100] and [010]. Thus, while the stress state is isotropic, the anisotropic elastic property of the crystal film breaks the rotational symmetry. As a result, an orthogonally oriented bi-directional pattern is predicted to dominate the initial growth of the wrinkles. By varying the ratio σ_2/σ_1 from 1 to 0, the growth spectrum changes from orthogonal to uniaxial in the direction of the major principal stress. The transition however depends on the principal angle θ_p. When $\theta_p = 0$, the growth spectrum remains orthogonal when the ratio σ_2/σ_1 slightly deviates from 1, but the peak growth rate becomes lower in one direction compared to the other. The growth spectrum becomes uniaxial as the lower peak diminishes for $\sigma_2/\sigma_1 < 0.8$. When $\theta_p = 45°$, the wave vectors corresponding to the peak growth rates rotate toward the direction of the major principal stress and eventually merge into a uniaxial pattern. At an intermediate stress ratio (e.g., $\sigma_2/\sigma_1 = 0.9$), four peaks lie on two directions of an oblique angle. Hence, the kinetically dominant wrinkle pattern at the early stage

becomes obliquely oriented bi-directional (e.g., zigzag pattern). This transition in the initial wrinkle patterns may be understood as a result of the competition between the material anisotropy and the stress anisotropy through $\overline{E}_\theta$ and σ_θ, respectively.

6. Equilibrium wrinkles

For a viscoelastic substrate layer with a rubbery modulus $\mu_R > 0$ at the long-time limit, wrinkling of an elastic film atop evolves towards an equilibrium state, dictated by minimization of the elastic strain energy stored in the film and the substrate. There may exist many mechanically equilibrium states, including the one at the reference state with no wrinkles at all. However, by the principle of thermodynamics these equilibrium states may be unstable, stable, or metastable. Searching for the thermodynamically equilibrium state with the minimum energy requires consideration of all possible wrinkle patterns. In practice, several simple wrinkle patterns (e.g., parallel stripes, checkerboard, and herringbone) have been considered for isotropic elastic films [36, 39]. However, experiments have commonly observed disordered wrinkle patterns (e.g., labyrinth). By the kinetics approach facilitated by the viscoelastic deformation in the substrate layer, evolution of wrinkle patterns can be simulated from a randomly generated initial perturbation, without *a priori* assumption of the wrinkle patterns. Since the viscoelastic deformation dissipates energy, the evolution process may be regarded as a searching algorithm for the minimum energy state, but it is not guaranteed that the global energy minimum can be reached. Nevertheless, the viscoelastic evolution represents a common physical process to form wrinkle patterns in experiments [17, 19, 51, 52], where the observed wrinkle patterns may also be trapped in a state of local energy minimum.

Consider a parallel-striped wrinkle pattern described by Eq. (51). The average strain energy per unit area of the film consists of three parts [33], namely

$$\overline{U}(A,k,\theta) = \overline{U}_C + \overline{U}_B + \overline{U}_S . \tag{56}$$

where

$$\overline{U}_C = \frac{1}{4}\sigma_\theta h k^2 A^2 + \frac{3}{64}\overline{E}_\theta h k^4 A^4 , \tag{57}$$

$$\overline{U}_B = \frac{1}{48}\overline{E}_\theta h^3 k^4 A^2 , \tag{58}$$

$$\overline{U}_S = \frac{1-\nu_s}{2(1-2\nu_s)} \frac{\mu_R}{H} A^2 . \tag{59}$$

The first two parts, $\overline{U}_C$ and $\overline{U}_B$, are associated with the in-plane deformation and bending of the elastic film, respectively, whereas $\overline{U}_S$ is the reversible elastic strain energy stored in the viscoelastic layer.

For an arbitrary wave vector, minimizing the total energy gives the equilibrium amplitude as a function of k and θ:

$$A_e(k,\theta) = \frac{2\sqrt{6}}{3k} \left[-\frac{\sigma_\theta}{\overline{E}_\theta} - \frac{(kh)^2}{12} - \frac{2(1-\nu_s)}{1-2\nu_s} \frac{\mu_R}{\overline{E}_\theta} \frac{1}{k^2 Hh} \right]^{1/2} . \tag{60}$$

Correspondingly, the total strain energy at the equilibrium state is also a function of k and θ, i.e., $\overline{U}_e(k,\theta) = \overline{U}(A_e, k, \theta)$. The spectra of the energy, $\overline{U}_e(k,\theta)$, are plotted in Figure 6 for both isotropic and anisotropic elastic films under various residual stress states. Similar to Figure 5, contours of the normalized strain energy, $\overline{U}_e/(C_{11}h)$, are plotted in the plane spanning the x and y components of the normalized wave vector; only negative energy values are plotted.
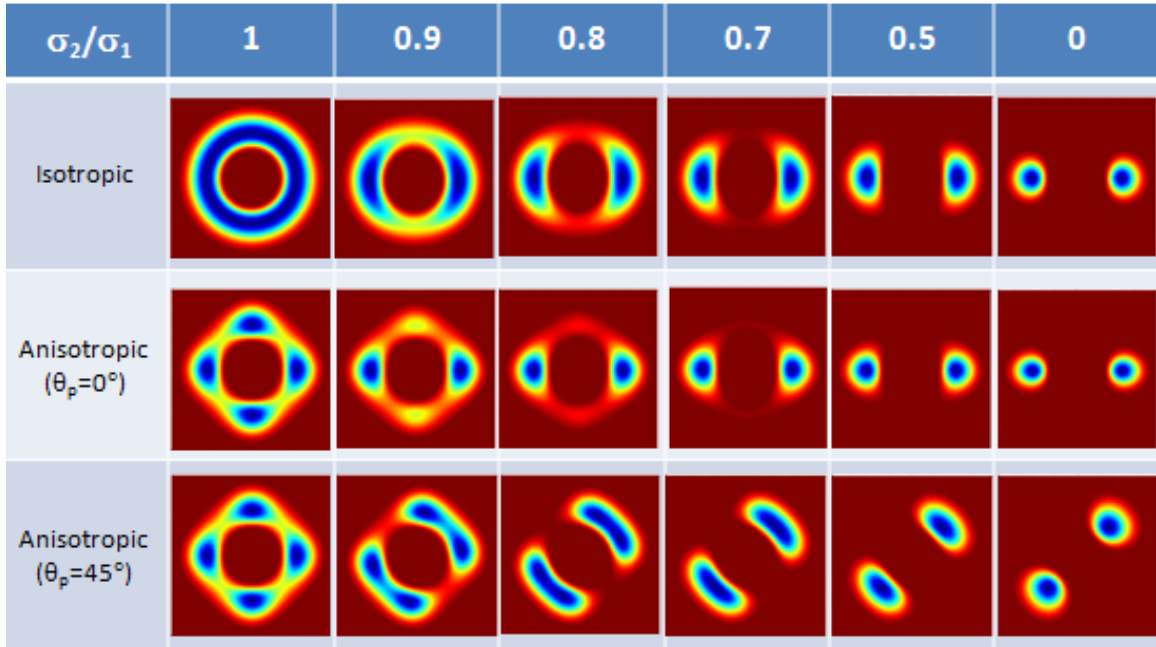

Figure 6. Energy spectra of parallel wrinkles at the equilibrium state for isotropic and anisotropic elastic films. The major principal stress is $\sigma_1/C_{11} = -0.003$.

For an isotropic elastic film, the energy contours are concentric circles under an equi-biaxial stress ($\sigma_2/\sigma_1 = 1$). The strain energy minimizes on a circle of a particular radius, with no favored direction due to rotational symmetry of the isotropic system. Once the ratio between the two principal stresses deviates from 1, the rotational symmetry is broken and the energy spectrum has two minima symmetrically located on the axis parallel to the direction of the major principal stress. Hence, an energetically favored wrinkle pattern emerges with parallel stripes perpendicular to the direction of the major principal stress. However, it should be noted that, since only parallel striped wrinkle patterns are considered in the present analysis, the energy minima in the spectra are not necessarily global minima. For example, it has been shown that herringbone and checkerboard wrinkle patterns may have lower energy than the parallel stripe pattern under an equi-biaxial stress state [36, 39].

For a cubic crystal film (e.g., SiGe), the energy spectrum depends on both the material anisotropy and the stress anisotropy. Under an equi-biaxial stress, there exist four energy minima aligned in the two orthogonal crystal directions, [100] and [010]. Thus, an energetically favored equilibrium wrinkle pattern would consist of parallel stripes in two orthogonal directions. When the two principal stresses are different, the energy spectrum depends on the principal direction θ_p. When $\theta_p = 0$, two energy minima are symmetrically located on the axis parallel to the direction of the major principal stress, while the other two minima in the orthogonal direction first become shallower and then disappear. When $\theta_p \neq 0$, as the stress ratio decreases from 1 to 0, the wave vectors of the energy minima first rotate toward the direction of the major principal stress and then merge to form two minima in the same direction. Therefore, different equilibrium wrinkle patterns may emerge as a transition between the orthogonal and the uniaxial patterns.

Furthermore, by minimizing the strain energy, $\overline{U}_e(k,\theta)$, with respect to k for a fixed angle θ, the equilibrium wavelength is obtained as a function of θ:

$$\lambda_e(\theta) = \frac{2\pi}{k_e(\theta)} = \pi h \left[\frac{2(1-2\nu_s)}{3(1-\nu_s)} \frac{H}{h} \frac{\overline{E}_\theta}{\mu_R} \right]^{1/4}. \tag{61}$$

Substitution of the equilibrium wavelength into Eq. (60) gives the equilibrium amplitude for the parallel wrinkles with the angle θ. Further minimization of the strain energy, $\overline{U}_e(k_e,\theta)$, with respect to θ gives the angle for the parallel wrinkles with the minimum energy. Both the equilibrium wavelength and the angle can be readily determined from the locations of the

minima in the energy spectrum shown in Figure 6. In particular, for an isotropic film under an equi-biaxial residual stress, the equilibrium wrinkle wavelength in (61) is independent of the angle, and the corresponding equilibrium wrinkle amplitude is

$$A_e = h \sqrt{\frac{2}{3}\left(\frac{\sigma_0}{\sigma_c} - 1\right)},$$ (62)

where σ_c is the critical stress given in Eq. (50). Recall that we have assumed a thin viscoelastic layer and $\nu_s < 0.5$. For a thick elastic substrate or $\nu_s = 0.5$, the equilibrium wrinkle wavelength and amplitude take different forms [37].

It is noted that, although the energy spectra in Figure 6 appear similar to the initial growth spectra in Figure 5, the locations for the energy minima are different from those of the maximum growth rates. While the fastest growing wavelength depends on the residual stress in the film, the equilibrium wrinkle wavelength is independent of the stress. In fact, the equilibrium wavelength is always greater than the fastest growing wavelength at the initial stage. Consequently, the wrinkle wavelength increases as the wrinkles evolve, a coarsening phenomenon that has been observed in experiments [19, 52]. A scaling analysis of coarsening is presented next in Section 7, which is confirmed by numerical simulations in Section 9.

7. Coarsening of wrinkles: a scaling analysis

As the wrinkle amplitude grows to be comparable to the film thickness, the residual stress in the film is partly relaxed, and the nonlinear effect of large deflection must be accounted for. It was found that there exists a kinetically constrained wrinkle state for each unstable wavelength [42]. In the neighborhood of such a state, the wrinkling process is very slow (i.e., $\frac{\partial w}{\partial t} \approx 0$), despite the fact that the film remains energetically unstable. For a particular wavelength ($\lambda > \lambda_c$), setting $\frac{\partial w}{\partial t} = 0$ and $R = 0$ in Eq. (43) leads to a spatially uniform stress in the film

$$\sigma_k = -\frac{4\pi^2 K}{\lambda^2 Fh} = -\frac{\pi^2 h^2 E_f}{3(1-\nu_f^2)\lambda^2}.$$ (63)

Correspondingly, the wrinkle amplitude is given by [42]

$$A_k = h\sqrt{\frac{1}{3}\left(\frac{\lambda^2}{\lambda_c^2}-1\right)}. \tag{64}$$

Therefore, the film stress can be continuously relaxed by increasing the wrinkle wavelength λ, i.e., coarsening. Meanwhile, the wrinkle amplitude grows.

Assume that the film stays in the neighborhood of the kinetically constrained state during coarsening, with both the wrinkle wavelength and the amplitude evolving nonlinearly. At this stage, the spatial distribution of the stress in the film is nearly uniform, approximately given by Eq. (63) as a function of the wrinkle wavelength. By comparing the first two terms in the right-hand side of Eq. (43), the time scale for this stage becomes

$$\tau_2 = \frac{K}{(Fh\sigma_k)^2} = \frac{\lambda^4}{16\pi^4 K}. \tag{65}$$

Thus, the wrinkle wavelength scales with the time as

$$\lambda \sim (Kt)^{1/4}. \tag{66}$$

The corresponding wrinkle amplitude can be obtained from Eq. (64). For $\lambda \gg \lambda_c$, the same scaling law applies for the growth of wrinkle amplitude, i.e., $A \sim (Kt)^{1/4}$.

Remarkably, a molecular dynamics (MD) simulation of buckling molecular chains showed a very similar scaling with the wavelength and the amplitude growing as a power of time: $\lambda \sim t^n$, $A \sim t^\beta$, where both the exponents nearly equal to 0.26 [53]. MD simulations of compressed solid membrane showed a similar coarsening dynamics with slightly larger exponents: $n = 0.28$ and $\beta = 0.29$ [54]. It has been noted that the nature of such dynamics is analogous to phase ordering phenomena such as spinodal decomposition [19].

Figure 7 schematically illustrates the three stages of wrinkling predicted for the wrinkle wavelength and amplitude: initial growth, coarsening, and equilibrium. The transition points can be determined approximately using the scaling laws [32]. First, the coarsening starts when the wrinkle reaches the kinetically constrained state of the fastest growing mode, which gives the first transition point:

$$t_1 = 4\tau_1 \ln\left(\frac{h}{\sqrt{3}A_0}\right), \tag{67}$$

where A_0 is the initial amplitude. Following the power law scaling for the wavelength coarsening, the second transition point is approximately

$$t_2 = t_1 \left(\frac{\lambda_e}{\lambda_m} \right)^4 = \frac{1}{R} \ln \left(\frac{h}{\sqrt{3} A_0} \right). \tag{68}$$

Therefore, the first transition time is proportional to the time scale of initial growth, which inversely scales with the square of the residual stress in the film, and the second transition time scales with the relaxation time $(1/R)$ of the viscoelastic layer, independent of the stress.
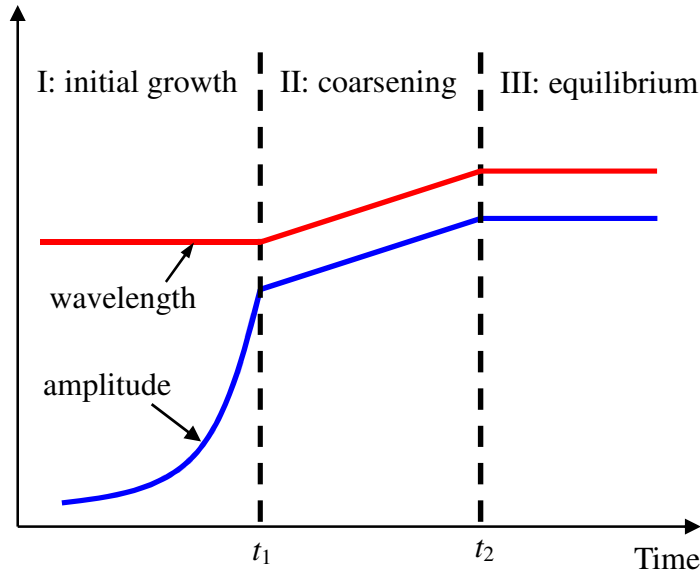
Figure 7. Schematic of the three-stage evolution of wrinkle wavelength and amplitude (both in log-log scale).

It should be noted that the above scaling analysis is based on the model assuming that the thickness of the viscoelastic layer is small compared to the wrinkle wavelength and that the viscoelastic layer is compressible (i.e., $v_s < 0.5$). Following the same approach, different scaling can be derived for the cases with incompressible thin layers or thick substrates [32]. For an incompressible, thin layer ($v_s = 0.5$), the evolution equation takes a different form (eq. 30), and the coarsening of the wrinkle wavelength scales as $\lambda \sim t^{1/6}$. For a thick viscoelastic substrate ($H/h \to \infty$), the scaling for coarsening is obtained as $\lambda \sim t^{1/3}$. It is thus speculated that, for a viscoelastic layer of finite thickness, the exponent of the power-law scaling for coarsening of

21

wrinkles should be between ¼ and 1/3 for a compressible layer and between 1/6 and 1/3 for an incompressible layer. Remarkably, a similar transition was noted for the phase separation kinetics of polymer blend films, where the coarsening exponent changes from 1 for thick films (100 nm) to a value near 0.5 for thin films (20 nm) [55].

8. A spectral method for numerical simulations

The nonlinear evolution equations of wrinkling in (41) and (42) can be solved numerically by a spectral method to simulate evolution of wrinkle patterns [32]. For convenience, the evolution equations are normalized by scaling the lengths, time, and stress components with the film thickness (h), the characteristic time for viscous flow (η_s/μ_f), and the shear modulus (μ_f), respectively. In addition, the linear and nonlinear terms are separated so that Fourier transform of the evolution equations takes the form

$$\frac{\partial \hat{w}}{\partial t} = B\hat{w} + \phi, \tag{69}$$

$$\frac{\partial \hat{u}_1}{\partial t} = C_1\hat{u}_1 + D_1\hat{u}_2 + \phi_1, \tag{70}$$

$$\frac{\partial \hat{u}_2}{\partial t} = C_2\hat{u}_1 + D_2\hat{u}_2 + \phi_2, \tag{71}$$

where a hat over a variable designates its Fourier transform with respect to the in-plane coordinates, and ϕ, ϕ_1, and ϕ_2 represent the nonlinear terms.

A semi-implicit algorithm is employed to integrate Eqs. (69)-(71) over time. First, using a backward finite difference scheme for the linear part and a forward scheme for the nonlinear part, Eq. (69) is integrated point-by-point in the Fourier space as

$$\hat{w}^{(n+1)} = \frac{\hat{w}^{(n)} + \phi^{(n)}\Delta t}{1 - B\Delta t}, \tag{72}$$

where Δt is the time step. The nonlinear terms are calculated in the real space and transformed to the Fourier space numerically by Fast Fourier transform (FFT).

Similarly, Eqs. (70) and (71) are integrated as

$$\hat{u}_1^{(n+1)} = \frac{(1 - D_2\Delta t)(\hat{u}_1^{(n)} + \phi_1^{(n)}\Delta t) + D_1\Delta t(\hat{u}_2^{(n)} + \phi_2^{(n)}\Delta t)}{(1 - C_1\Delta t)(1 - D_2\Delta t) - C_2D_1(\Delta t)^2}, \tag{73}$$

$$\hat{u}_2^{(n+1)} = \frac{(1 - C_1 \Delta t)(\hat{u}_2^{(n)} + \phi_2^{(n)} \Delta t) + C_2 \Delta t (\hat{u}_1^{(n)} + \phi_1^{(n)} \Delta t)}{(1 - C_1 \Delta t)(1 - D_2 \Delta t) - C_2 D_1 (\Delta t)^2} . \tag{74}$$

The advantage of the spectral method is that it resolves the challenges in the numerical simulations by converting the high-order spatial differentiations in the real space into algebraic multiplications in the reciprocal Fourier space, utilizing the efficiency of FFT and its inverse to communicate between the two spaces. Similar methods have been used for simulations of other evolution systems [56-58].

Numerically, a square computational cell in the $x - y$ plane with a periodic boundary condition is used. The size of the computational cell is selected such that it is sufficiently large compared to the longest wrinkle wavelengths (i.e., the equilibrium wavelength λ_e), thus minimizing the effect of cell size on the numerical results. The cell is discretized into grids in both the x and y directions with a sufficient resolution in space to resolve the shortest wavelength of interest (i.e., the critical wavelength λ_c). Moreover, the semi-implicit algorithm for time integration is conditionally stable. To insure numerical stability and convergence, the time step Δt (normalized by η_s / μ_f) must be sufficiently small.

9. Numerical simulations of wrinkle patterns

In this section, results from numerical simulations are presented to show evolution of diverse wrinkle patterns. For quantitative characterization of the wrinkle patterns, which may be ordered or disordered, two quantities are calculated. First, the wrinkle amplitude is evaluated by a root-mean-square (RMS) of the deflection, namely

$$\text{RMS}(t) = \sqrt{\frac{\sum w(m, n, t)^2}{N^2}} , \tag{75}$$

where $w(m, n, t)$ is the deflection of the grid point (m, n) at time t and N is the number of grid points along each side of the computational cell. Second, the average wrinkle wavelength is evaluated by

$$\bar{\lambda}(t) = \frac{2\pi}{\bar{k}(t)} , \tag{76}$$

where

$$\bar{k}(t) = \sqrt{\frac{\sum |\hat{w}(m,n,t)|^2 k(m,n)^2}{\sum |\hat{w}(m,n,t)|^2}} \ . \tag{77}$$

Equation (77) may be regarded as a weighted RMS of the wavenumbers in the Fourier space, where the weight $|\hat{w}|^2$ represents the power intensity of the corresponding wavenumber, similar to the power spectra in experiments [19].
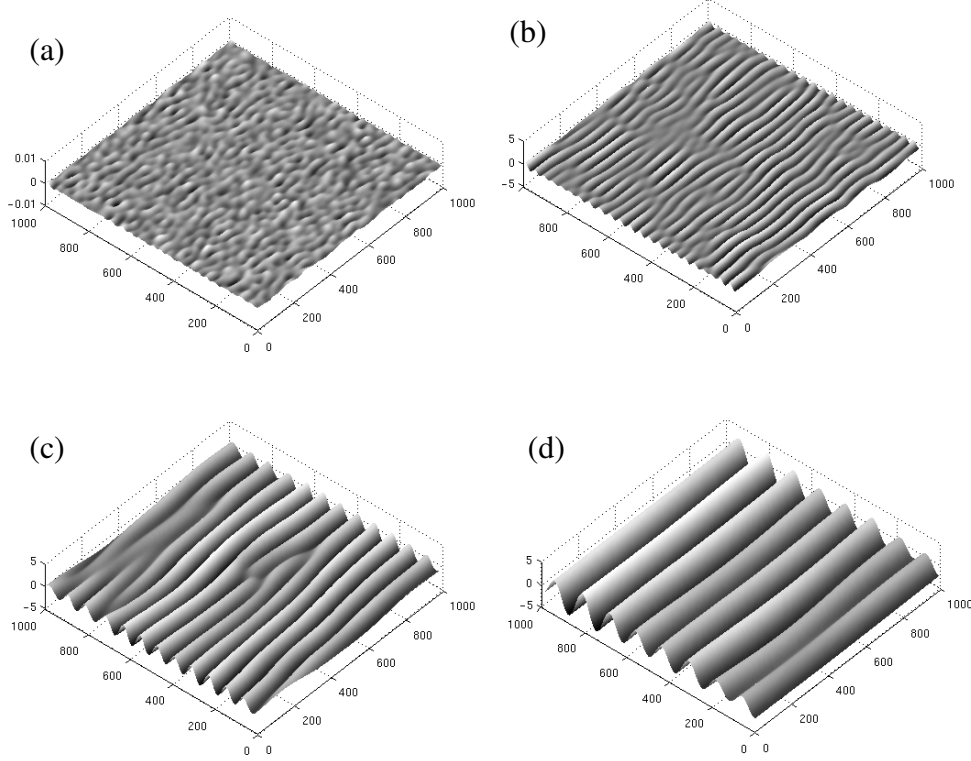

Figure 8. A simulated evolution sequence of wrinkles in a uniaxially stressed film. (a) $t = 10^4$: $\bar{\lambda} = 46.2$ and RMS = 0.00033; (b) $t = 10^5$: $\bar{\lambda} = 44.4$ and RMS = 0.313; (c) $t = 10^6$: $\bar{\lambda} = 77.8$ and RMS = 0.947; (d) $t = 10^7$: $\bar{\lambda} = 128.2$ and RMS = 1.66.

9.1 Uniaxial wrinkles (parallel stripes)

Figure 8 shows an evolution sequence of simulated wrinkle patterns under a uniaxial stress with magnitude $\sigma_0 = 0.01$ (normalized by the shear modulus μ_f). Here the film is isotropic and the modulus ratio μ_R / μ_f is set to zero. The other parameters are: $H/h = 10$, $\nu_s = 0.45$, and $\nu_f = 0.3$. The computational cell size is $L/h = 1000$, with a 128 by 128 grid. The

normalized time step is $\Delta t = 100$. To start the simulation, a random perturbation of amplitude $0.001h$ is introduced over the entire computational cell.

Under the uniaxial stress, a parallel stripe pattern emerges quickly in the direction perpendicular to the stress. Both the wrinkle amplitude and the wavelength increase with time. The presence of dislocation-type defects in the parallel stripe pattern is evident in Fig. 8 (b) and (c). The defect density decreases as the wrinkle evolves. Similar results are obtained for various stress magnitudes. Figure 9 plots the evolution of the average wrinkle wavelength and the RMS amplitude. The average wavelength quickly reaches a plateau at a level depending on the residual stress, corresponding to the fastest growing mode predicted by Eq. (48) for the initial growth. Meanwhile, the RMS amplitude increases exponentially, as predicted by Eq. (49). The wavelength starts to increase (i.e., coarsening) when the RMS reaches a critical level (~ 0.4), nearly independent of the residual stress. As indicated by the horizontal dashed line in Fig. 9b, the RMS at the kinetically constrained state of wavelength $\lambda = \lambda_m$ is 0.408, which is close to the transition points for all stresses. Therefore, the first transition time in Eq. (67) is a reasonable estimate for onset of coarsening.
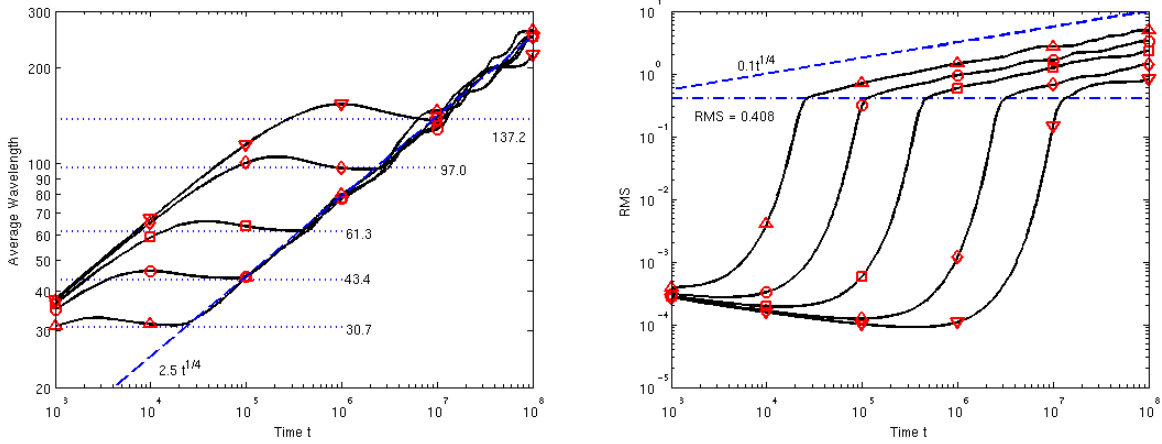

Figure 9. Evolution of average wrinkle wavelength and RMS amplitude under uniaxial stresses ($\mu_R / \mu_f = 0$): $\sigma_0 = 0.02$ (Δ), 0.01 (o), 0.005 ($\square$), 0.002 ($\Diamond$), 0.001 (∇). The horizontal dotted lines in (a) indicate the fastest growing wavelengths predicted by the linear perturbation analysis. The dot-dashed line in (b) corresponds to the stress-independent RMS at the kinetically constrained state of the fastest growing mode.

During coarsening, the wavelength follows a straight line with a slope $1/4$ in the log-log plot as shown in Fig. 9a, in good agreement with the scaling analysis in Eq. (66). Interestingly, in spite of the different residual stresses and different transition points, the wrinkle wavelength follows essentially the same path of coarsening. On the other hand, the wrinkle amplitude grows with the same scaling (after a short transition period) but with different magnitudes for different residual stresses. Since no elastic equilibrium state exists for the present case ($\mu_R / \mu_f = 0$), the coarsening process continues until the simulation is stopped at $t = 10^8$.
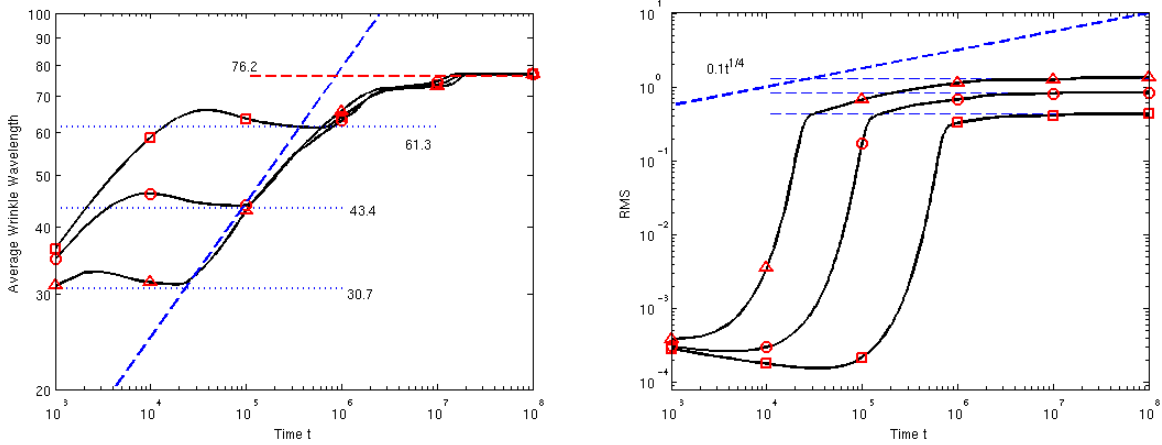
Figure 10. Evolution of average wrinkle wavelength and RMS amplitude under uniaxial stresses: $\sigma_0 =$ 0.02 (Δ), 0.01 (o), 0.005 ($\square$), with a modulus ratio $\mu_R / \mu_f = 10^{-5}$. The equilibrium wavelength is indicated by the horizontal dashed line in (a), and the equilibrium amplitudes are indicated by the horizontal dashed lines in (b).

The substrate elasticity has two effects on the wrinkling process. First, it can stabilize the film under small stresses so that the film remains flat with no wrinkles at all. The critical stress is given by Eq. (50). The second effect is that, when the residual stress is high enough to cause wrinkling, the elastic limit of the substrate will eventually stabilize the wrinkle pattern. For parallel stripe wrinkles, the equilibrium wrinkle wavelength and amplitude are analytically predicted in Eqs. (61) and (62), respectively. Figure 10 plots evolution of the average wrinkle wavelength and the RMS amplitude from numerical simulations under uniaxial stresses and with a modulus ratio, $\mu_R / \mu_f = 10^{-5}$. The critical stress in this case is $\sigma_c = 0.00324$. When $\sigma_0 < \sigma_c$, no wrinkle grows. For $\sigma_0 > \sigma_c$, the initial growth is similar to those in Figure 9, but with a slower

growth rate as predicted by the linear perturbation analysis [31]. The coarsening, however, is influenced by the presence of an equilibrium state. The wrinkle wavelength increases and eventually reaches a plateau, in agreement with the predicted equilibrium wavelength, $\lambda_e = 76.2$ in this case. At the same time, the RMS amplitude approaches a plateau in agreement with the predicted equilibrium amplitude. While the equilibrium wavelength is independent of the residual stress, the equilibrium amplitude increases as the stress magnitude increases. Apparently, the power-law scaling for coarsening becomes less predictive as the wrinkles approach the equilibrium state. As a result, the second transition time predicted by Eq. (68) typically underestimates the time to reach the equilibrium state.
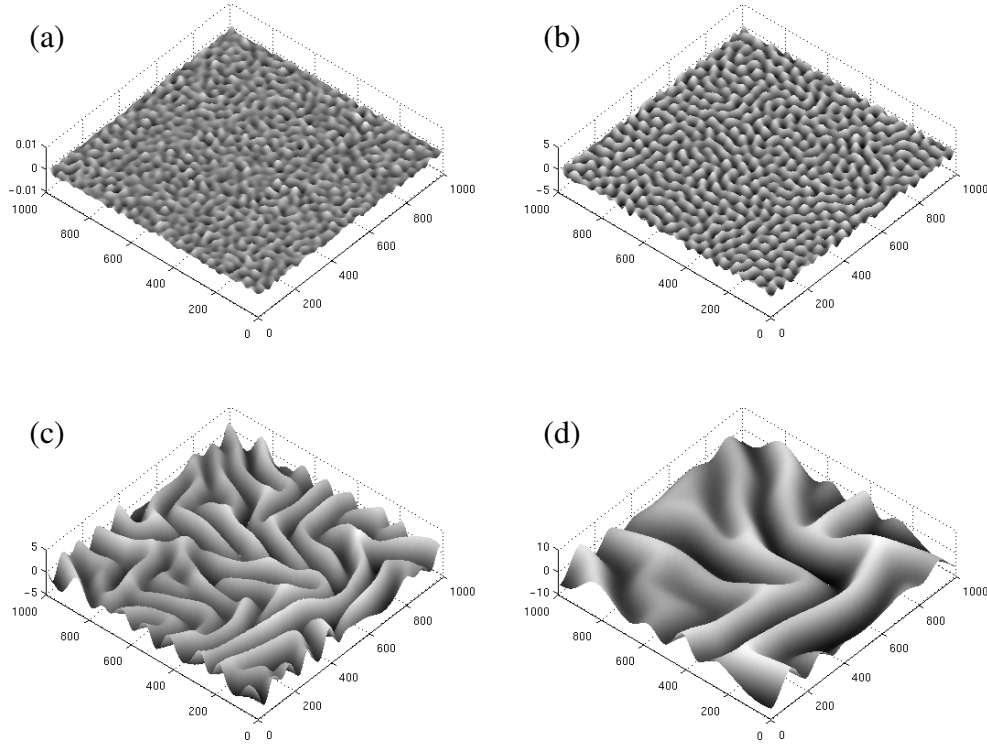

Figure 11. A simulated evolution sequence of wrinkles in an equi-biaxially stressed film. (a) $t = 10^4$: $\overline{\lambda} = 42.8$ and RMS = 0.00054; (b) $t = 10^5$: $\overline{\lambda} = 45.1$ and RMS = 0.423; (c) $t = 10^6$: $\overline{\lambda} = 98.4$ and RMS = 1.50; (d) $t = 10^7$: $\overline{\lambda} = 196.9$ and RMS = 3.18.

9.2 Isotropic wrinkles (labyrinths)

Figure 11 shows an evolution sequence of simulated wrinkle patterns under an equi-biaxial stress of magnitude $\sigma_0 / \mu_f = 0.01$ with $\mu_R / \mu_f = 0$. Differing from the parallel stripe patterns under uniaxial stresses, an isotropically disordered labyrinth pattern emerges under the

equi-biaxial stress, due to the rotational symmetry in the isotropic system. Figure 12 plots the evolution of the average wrinkle wavelength and the RMS amplitude. Similar to the cases under uniaxial stresses, the average wavelength quickly reaches a plateau, corresponding to the fastest growing mode predicted by the linear analysis, and the RMS increases exponentially during the initial growth stage. The RMS at the transition point from initial growth to coarsening is about the same too, but the transition process is different for the wrinkle wavelength. The coarsening of the wavelength is faster immediately after it reaches the transition point, giving a slope larger than ¼ in the log-log plot (Fig. 12a). The slope then decreases as coarsening continues, eventually approaching ¼, as predicted by the scaling analysis. Such a behavior may be attributed to the disorder in the labyrinth wrinkle pattern. At the early stage, the pattern is highly disordered with relatively short stripes in random directions, for which the coarsening is not well described by the scaling law for parallel stripe patterns. Later on, while the wrinkle pattern remains disordered, it consists of long stripes coarsening in a similar manner as parallel stripes. Consequently, the coarsening paths under equi-biaxial stresses are different for different resdiual stresses, and they are different from those under uniaxial stresses.
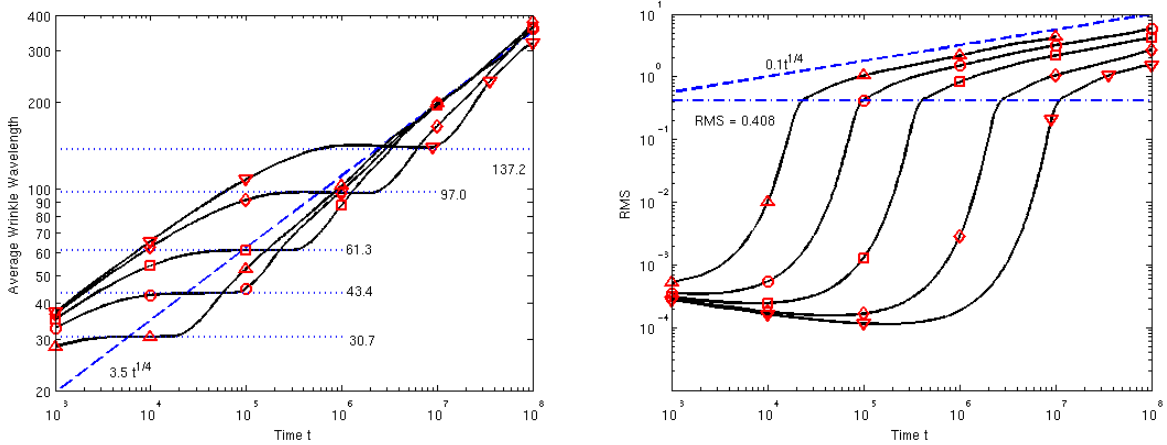

Figure 12. Evolution of average wrinkle wavelength and RMS amplitude under equi-biaxial stresses: $\sigma_0 = 0.02\ (\Delta),\ 0.01\ (o),\ 0.005\ (\square),\ 0.002\ (\Diamond),\ 0.001\ (\nabla)$, with $\mu_R / \mu_f = 0$.

Using the length scale L_1 and the time scale τ_1 as defined in (45) and (46), respectively, Figure 13 re-plots the evolution of wrinkle wavelength from the numerical simulations (Figs. 9a and 12a, with $\mu_R / \mu_f = 0$). Remarkably, the evolution paths for different stress magnitudes collapse onto one for uniaxial stresses and another for equi-biaxial stresses. At the early stage,

the film selects the fastest growing wrinkle wavelength, which is the same for both uniaxial and equi-biaxial stresses. Interestingly, the process of wavelength selection at the early stage seems to follow the same scaling law as coarsening, i.e., $\lambda \sim t^{1/4}$. This process, however, may depend on the initial perturbation, and is typically too short to be observed in experiments. The two paths are slightly different in the transition to coarsening. Under uniaxial stresses, the coarsening process is well described by the power-law scaling. Under equi-biaxial stresses, however, it undergoes a transition stage with a faster coarsening rate before it approaches the same power law. This is consistent with the MD simulations of buckling molecular chains [53] and membranes [54], with the chains under uniaxial stresses and the membranes under equi-biaxial stresses.
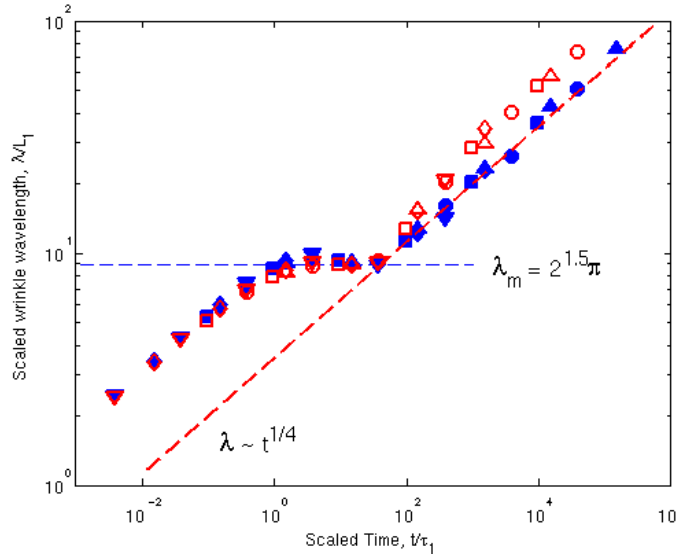

Figure 13. Evolution of wrinkle wavelength, scaled by the length L_1 and the time τ_1, under different uniaxial stresses (solid symbols) and equi-biaxial stresses (open symbols).

By adding substrate elasticity ($\mu_R / \mu_f > 0$), the average wrinkle wavelength and the RMS amplitude eventually saturate at the equilibrium state [32], similar to the uniaxial wrinkles as shown in Fig. 10. Figure 14 shows the wrinkle patterns for different stresses at the end of each simulation ($t = 10^8$) when the system has reached a nearly equilibrium state. Under uniaxial stresses (Fig. 14a), similar patterns with parallel stripes are obtained for different stress magnitudes, with the same wrinkle wavelength but different amplitudes. Under equi-biaxial stresses (Fig. 14, b-d), although the average wavelength at equilibrium is independent of the

residual stress, the coarsening dynamics leads to different evolution paths and thus different wrinkle patterns. Interestingly, the isotropic wrinkle patterns seem to organize into a domain structure, with parallel stripes in each domain, while the domain size decreases as the stress magnitude increases. The details of the equilibrium wrinkle pattern under equi-biaxial stresses may depend on the initial random perturbation, but the average wrinkle wavelength and the RMS amplitude are insensitive to the initial perturbation. Thus, the apparently chaotic pattern may be characterized by the two deterministic quantities.
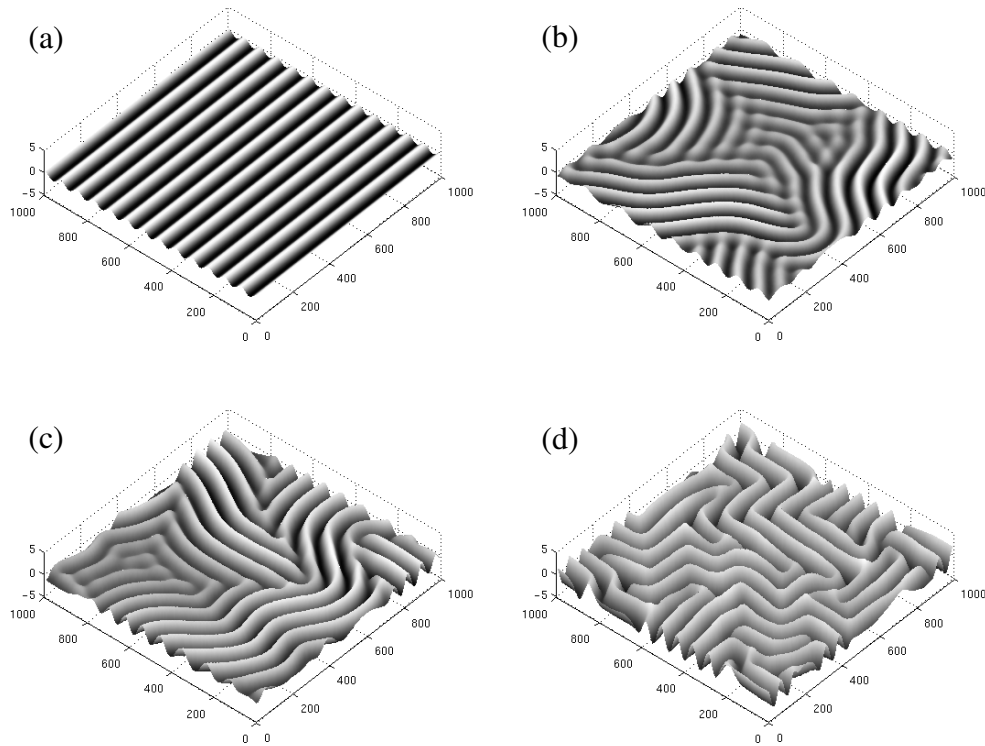

Figure 14. Nearly equilibrium wrinkle patterns: (a) under a uniaxial stress, $\sigma_0 = 0.005$; (b)-(d) under equi-biaxial stresses, $\sigma_0 = 0.005$, 0.01, and 0.02.

In addition to the labyrinth pattern, checkerboard and herringbone patterns have also been considered as the possible equilibrium wrinkle patterns under equi-biaxial stresses [36, 39, 40]. As shown in Fig. 15a, by the kinetics approach, a checkerboard pattern is obtained when the equi-biaxial residual stress is slightly above the critical stress for onset of wrinkling. A transition from the checkerboard pattern to the labyrinth pattern occurs as the stress magnitude increases. Such a transition may be attributed to a geometric origin [37]: a flat film can bend to a

cylindrical surface with no stretching, but bend to a spherical cap with severe stretching at the crest. Starting from a flat film with a small random perturbation, wrinkles emerge randomly at the early stage, forming shallow spherical dimples. As the wrinkle amplitude grows, the spherical dimples elongate to form cylindrical ridges. The competition between bending and stretching leads to the transition from spherical dimples to cylindrical ridges, while the overall rotational symmetry is maintained as the cylindrical ridges form an isotropic labyrinth pattern. When the residual stress is low, the equilibrium wrinkle amplitude is small, and the shallow spherical dimples remain at the equilibrium state to form the checkerboard pattern. Such an ordering however may be an artifact of the square-shaped computational cell used in the numerical simulation. In a recent experiment, hexagonally packed dimples have been observed [59, 60], which manifests the rotational symmetry in the isotropic system. Figure 15(b) shows a herringbone pattern, which is macroscopically isotropic. Such a pattern appears to be a special case of the labyrinth pattern, with locally ordered parallel stripes and a parallel domain structure. Alternatively, it may also be considered as a combination of the checkerboard pattern (spherical dimples) and the parallel stripe pattern [61]. It was found that, among the three ordered wrinkle patterns (parallel stripes, checkerboard, and herringbone), the herringbone pattern yields the lowest elastic energy in an equi-biaxially compressed film at relatively large overstresses [36, 39]. Recently, Cai et al. [60] presented an energetic analysis that predicts the transition stress from the checkerboard pattern to the herringbone pattern under equi-biaxial compression. They also suggested that, with a small initial curvature of the film, the hexagonal pattern has a lower elastic energy than the checkerboard pattern at small overstresses.
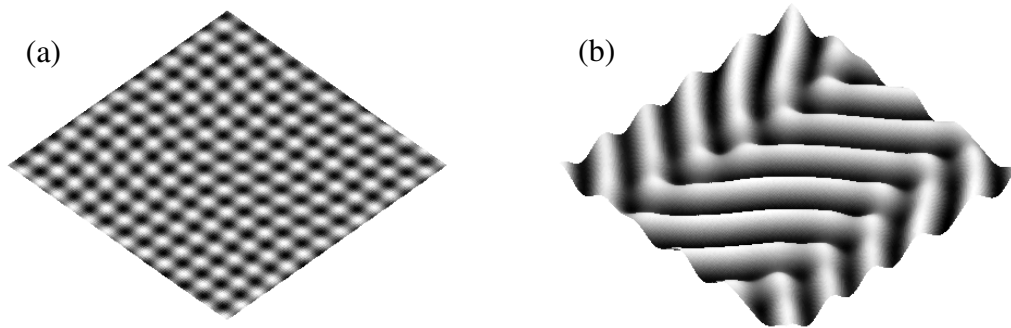

Figure 15. Ordered wrinkle patterns under equi-biaxial compression: (a) Checkerboard pattern; (b) Herringbone pattern.

9.3 Transition of wrinkle patterns: secondary buckling instability

Apparently, the equilibrium wrinkle patterns in an isotropic elastic film depend sensitively on the residual stress at the reference state. A uniaxial stress results in a parallel stripe wrinkle pattern, and an isotropically disordered labyrinth pattern often emerges under an equi-biaxial residual stress. In between, when the film is subject to a generally biaxial stress, a transition is expected as the ratio between the two principal stresses (σ_2/σ_1) varies from 0 to 1. In particular, while wrinkles in the parallel stripe pattern effectively relax the compressive stress in one direction, the presence of a compressive stress in the perpendicular direction may induce a secondary buckling instability that leads to the transition of wrinkling patterns [34, 40].

Consider a perturbation to the parallel wrinkles, with the out-of-plane displacement taking the form

$$w(x, y, t) = A\cos\{k_1[x + B\cos(k_2 y)]\}.$$

(78)

The elastic strain energy of the system consists of the bending and in-plane strain energy in the film and the elastic energy in the substrate [34]:

$$\overline{U}_B = \frac{E_f h^3}{48(1-v_f^2)} k_1^2 A^2 \left(k_1^2 + k_1^2 k_2^2 B^2 + \frac{1}{2} k_2^4 B^2 + \frac{3}{8} k_1^2 k_2^4 B^4 \right),$$

(79)

$$\overline{U}_C = \frac{h}{2E_f}\left(\sigma_1^2 + \sigma_2^2 - 2v_f \sigma_1 \sigma_2\right)$$

$$+ \frac{1}{8} hA^2 k_1^2 \left(2\sigma_1 + \sigma_2 B^2 k_2^2\right) + \frac{3E_f}{64(1-v_f^2)} hA^4 k_1^4 \left(1 + v_f B^2 k_2^2 + \frac{3}{8} B^4 k_2^4\right),$$

(80)

$$\overline{U}_S = \frac{1}{2}\frac{1-v_s}{(1-2v_s)}\frac{\mu_R}{H}A^2.$$

(81)

The total strain energy is

$$\overline{U}_{total} = \overline{U}_B + \overline{U}_C + \overline{U}_S = \overline{U}(A, k_1) + \Delta\overline{U}(A, B, k_1, k_2).$$

(82)

The first term on the right-hand side of Eq. (82) is the strain energy for parallel wrinkles, for which the equilibrium amplitude and wavelength are obtained in Section 6. The secondary buckling amplitude (B) and the wavenumber (k_2) are then obtained by minimizing the second term, which is

$$\Delta\overline{U} = \frac{(|\sigma_1|-\sigma_c)^2 h}{36\overline{E}_f}\left[\frac{\overline{E}_f k_2^2 h^2}{|\sigma_1|-\sigma_c} - 12\left(\frac{|\sigma_2|-\sigma_c}{|\sigma_1|-\sigma_c} - v_f\right)\right]k_2^2 B^2 + O(B^4).$$

(83)

32

The leading term on the right-hand side of Eq. (83) is quadratic of the amplitude B. When the coefficient is negative, the total energy in (82) decreases with the amplitude B, and thus the parallel wrinkles become unstable. The critical condition for the seconding buckling is then predicted as

$$\frac{|\sigma_2| - \sigma_c}{|\sigma_1| - \sigma_c} = \nu_f . \tag{84}$$

The same result was obtained by Audoly and Boudaud [40] using a different perturbation function. Apparently, Poisson's ratio of the film plays an important role for the secondary buckling.
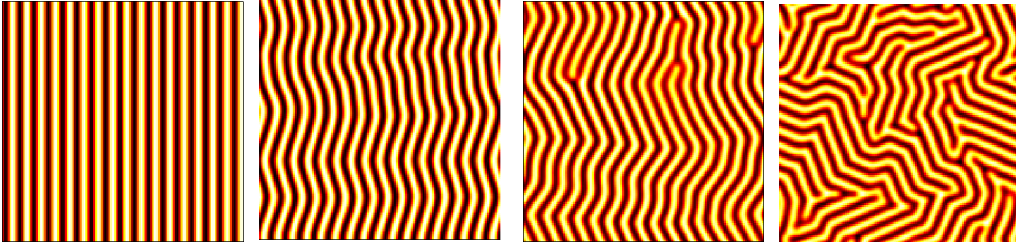

Figure 16. Transition of wrinkle patterns for an isotropic elastic film, from parallel stripes to zigzag and to labyrinth, subject to biaxial residual stresses with $\sigma_1 / \overline{E}_f = -0.005$ and $\sigma_2 / \overline{E}_f = -0.0028$, -0.0032, -0.0035, -0.005 (from left to right).

By the kinetics approach, evolution of wrinkle patterns under biaxial stresses is simulated. Figure 16 shows the near-equilibrium wrinkle patterns obtained from numerical simulations. The major principal stress is identical in all simulations ($\sigma_1 = -0.005\overline{E}_f$) while σ_2 varies between zero to σ_1. The following parameters were used: $\mu_R / \overline{E}_f = 10^{-5}$, $\nu_f = 0.3$, $\nu_s = 0.45$, and $H/h = 10$. The critical stress for onset of wrinkling (Eq. 50) in this case is $\sigma_c = 0.0019\overline{E}_f$, and the transition stress predicted by Eq. (84) is $\sigma_2 = -0.00284\overline{E}_f$. Therefore, when $0 > \sigma_2 > -0.00284\overline{E}_f$, parallel wrinkles form and they are stable. When $-0.00284\overline{E}_f > \sigma_2 > \sigma_1$, parallel wrinkles become unstable and zigzag wrinkle patterns emerge. The wavelength of the zigzag and its amplitude may be predicted by energy minimization including the high-order terms in (83). Due to the relatively long zigzag wavelength, a much larger computational cell is needed to eliminate the effect of cell size on the simulated zigzag

patterns. Nevertheless, the numerical simulations clearly demonstrate the transition from the parallel stripe pattern to the zigzag pattern. As σ_2 approaches σ_1, the zigzag wrinkle pattern becomes increasingly disordered with defects. When $\sigma_2 = \sigma_1$, the wrinkles become isotropically disordered in a labyrinth pattern.

Transition of wrinkle patterns has been observed experimentally [11, 62, 63]. By sequential stretch and release, Lin and Yang [63] reported reversible transition of wrinkle patterns from parallel stripes to zigzag and to highly ordered herringbone patterns. In their experiments, a square-shaped polydimethylsiloxane (PDMS) strip was first stretched equi-biaxially and then treated with oxygen plasma to form a thin oxide layer at the surface. Next, the pre-stretch was released either sequentially in the x and y directions or simultaneously in both directions. By the sequential release, they observed a transition in the wrinkle pattern from parallel stripes to zigzag, which qualitatively agrees with the secondary buckling analysis and the numerical simulations shown in Fig. 16. Interestingly, a highly ordered herringbone pattern was obtained at the end of the sequential release when the oxide layer was under equi-biaxial compression. On the other hand, by simultaneous release, a disordered labyrinth pattern was obtained at the same final state of equi-biaxial compression. Apparently, the wrinkle pattern depends on the loading path in these experiments. The well-ordered parallel wrinkles formed during the first stage of sequential release seem to have placed seeding for the ordering of subsequent wrinkle patterns. Without any seeding, wrinkles grow in all directions during the simultaneous release, resulting in a disordered labyrinth pattern. Indeed, to obtain the herringbone pattern by numerical simulations as shown in Fig. 15(b), the residual stress in the film was assumed to be time-dependent to simulate a sequential loading so that parallel wrinkles formed first to be followed by zigzag and eventually herringbone patterns. Otherwise, disordered labyrinth patterns emerge from a random initial perturbation under equi-biaxial compression, as shown in Figs. 11 and 14. The path-dependent wrinkle patterns suggest that there may exist more than one equilibrium states (ordered and disordered) although some of them may be thermodynamically metastable. As such, by controlling the loading path, ordered wrinkle patterns can be achieved.
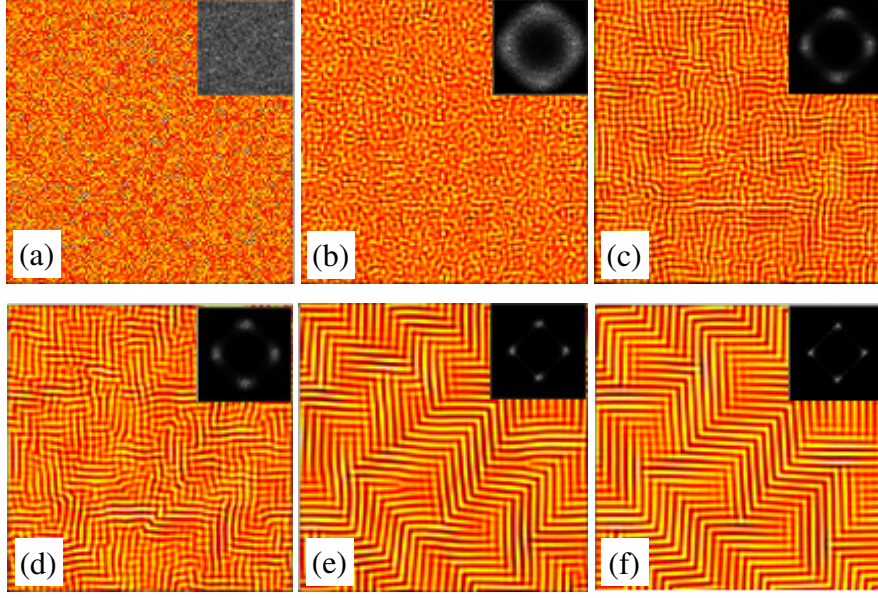
Figure 17. A simulated evolution sequence of the wrinkle pattern for a SiGe crystal film under an equi-biaxial residual stress ($\sigma_1 = \sigma_2 = -0.003C_{11}$): (a) $t = 0$, RMS = 0.0057, $\bar{\lambda}$ = 38.83; (b) $t = 10^5$, RMS = 0.0165, $\bar{\lambda}$ = 44.77; (c) $t = 5 \times 10^5$, RMS = 0.4185, $\bar{\lambda}$ = 47.06; (d) $t = 10^6$, RMS = 0.4676, $\bar{\lambda}$ = 50.75; (e) $t = 10^7$, RMS = 0.5876, $\bar{\lambda}$ = 56.43; (f) $t = 10^8$, RMS = 0.5918, $\bar{\lambda}$ =56.63.

9.4 Wrinkle patterns of anisotropic crystal films

Most of the theoretical studies on wrinkling have assumed isotropic, linear elastic properties for the film. Several experimental studies have reported wrinkling of anisotropic crystal films. Hobart et al. [51] observed wrinkling of single-crystal silicon-germanium (SiGe) alloy films on a glass layer when annealed at an elevated temperature, where SiGe is a cubic crystal with anisotropic elastic properties. More detailed experiments [52] showed that the SiGe film preferentially wrinkles in two orthogonal directions, closely aligned with the <100> axes of the crystal film. Similar orthogonal patterns were observed for a SiGe/oxide film stack [64]. On the other hand, Choi et al. [9] observed zigzag wrinkle patterns of single-crystal Si films bonded to a PDMS substrate, where the jog angle of the zigzag was close to 90°, although no alignment with the crystal axes was reported. By the kinetics approach, coupled with the equilibrium equations for an anisotropic thin film (Section 2), wrinkle patterns of anisotropic crystal films can be simulated under various stress states [33]. In particular, the effects of anisotropic elastic property of a cubic crystal film on wrinkle patterns at both the initial growth stage and the equilibrium state have been elucidated by the analytical solutions in Sections 5 and 6,

35

respectively. By the spectral method (Section 8), Figure 17 shows an evolution sequence of the simulated wrinkle pattern for a cubic crystal film (SiGe) under an equi-biaxial compression ($\sigma_1 = \sigma_2 = -0.003 C_{11}$). Here, a square computational cell of size $L = 2000h$ is discretized into a 128 by 128 grid, with periodic boundary conditions. A random perturbation of amplitude $0.01h$ was introduced as the initial perturbation from the reference state. The deflection, $w(x, y, t)$, is normalized by the film thickness h and plotted as contours in the x-y plane; the time is normalized by the time scale $\tau = \eta / C_{11}$. The insets in Figure 17 show contours in the Fourier space as the Fourier transform of the corresponding wrinkle patterns.

As shown in Fig. 17, the initial perturbation at $t = 0$ is featureless, with a small roughness (RMS = 0.0057). At $t = 10^5$, the RMS amplitude has grown significantly, and the Fourier transform takes a shape similar to the growth-rate spectrum shown in Figure 5 for the anisotropic film under an equi-biaxial stress. At the early stage, many Fourier components are growing simultaneously, resulting in a disordered wrinkle pattern. The average wrinkle wavelength ($\bar{\lambda} = 44.77$) is close to the fastest growing wavelength ($\lambda_{\theta m} = 43.23$ for $\theta = 0$) as predicted by the linear analysis. At $t = 5 \times 10^5$, the Fourier components with the fastest growth rate start to dominate, and the wrinkles become increasingly aligned in the two orthogonal directions of the crystal, [100] and [010]. At $t = 10^6$, the wrinkle pattern exhibits a bi-phase domain structure, with parallel stripes locally ordered in one of the two orthogonal directions in each domain. Further evolution of the wrinkle pattern shows two coarsening processes. First, the wavelength of each individual wrinkle stripe increases. As a result, the average wavelength of the wrinkle over the entire area increases, similar to the coarsening process of an isotropic film. Furthermore, the orthogonal bi-phase domain structure of the wrinkle pattern evolves with coarsening of the domain size, as can be seen clearly from $t = 10^6$ to $t = 10^7$. Both the wrinkle wavelength and the domain size seem to saturate after a long time evolution. It is thus postulated that the viscoelastic evolution process seeks to minimize the total strain energy in the film and the substrate not only by selecting an equilibrium wavelength for individual wrinkle stripes but also by selecting a particular domain size [33]. The present simulation of the wrinkle pattern evolution qualitatively agrees with the experiments by Peterson [52] for a SiGe film on a glass layer at an elevated temperature. The orthogonally ordered wrinkle pattern is also comparable to the wavy structures observed in biaxially stressed silicon membranes on a PDMS substrate [9].
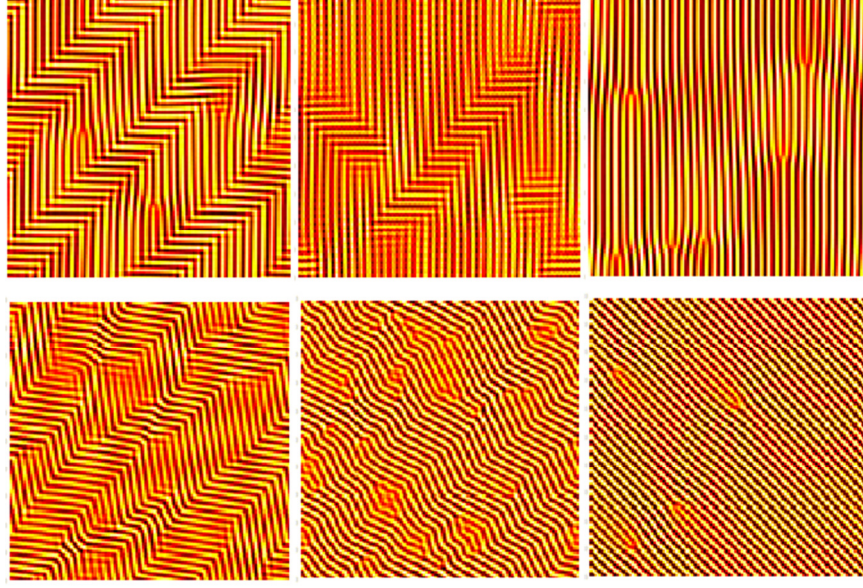
Figure 18. Transition of wrinkle patterns for an anisotropic crystal film, from orthogonal to uniaxial, under biaxial stresses with $\theta_p = 0$ (upper row) and $\theta_p = 45°$ (lower row). From left to right: $\sigma_2/\sigma_1 = 0.9$, 0.8, and 0.7.

Subject to a generally biaxial stress, the wrinkle pattern depends on the stress anisotropy in addition to the material anisotropy. Similar to the isotropic film, the wrinkle pattern undergoes a transition from the orthogonal pattern under an equi-biaxial stress to the parallel stripe pattern under a uniaxial stress. However, the transition path for the anisotropic film depends on the principal direction of the residual stress [33]. Figure 18 shows the wrinkle patterns with two different principal directions. When $\theta_p = 0$, the directions of principal stresses coincide with the <100> crystal axes. In this case, the orthogonal wrinkle pattern remains orthogonal as the stress ratio σ_2/σ_1 slightly deviates from 1, but the bi-phase domain structure changes. Under the equi-biaxial stress ($\sigma_2/\sigma_1 = 1$), the parallel wrinkles are equally distributed in the two orthogonal directions. For $\sigma_2/\sigma_1 = 0.9$, the area decorated with wrinkles in the [100] direction is greater than the area decorated by wrinkles in the [010] direction. As the stress ratio σ_2/σ_1 decreases further, the area percentage of the [100] wrinkles increases, and the entire area is covered with the [100] wrinkles when $\sigma_2/\sigma_1 < 0.8$. Thus, the orthogonal wrinkle pattern changes to the uniaxial pattern by eliminating one of the two phases as the stress anisotropy increases. When

37

$\theta_p = 45°$, the directions of the principal stresses are in the <110> directions of the crystal. As a result, the uniaxial wrinkles are parallel to the <110> directions, which are absent in the orthogonal pattern under an equi-biaxial stress. As the stress ratio decreases, the directions of the wrinkle stripes first rotate to form zigzag patterns and then merge into the [110] direction for $\sigma_2 / \sigma_1 < 0.8$. Thus, the transition occurs by rotating the wrinkles in both phases towards the major principal direction. Note that the zigzag pattern in transition typically consists of wrinkle stripes in two directions of an oblique angle, consistent with the rotation of the energy minima in the predicted energy spectra (Fig. 6). Therefore, the competition between the stress anisotropy and the material anisotropy further enriches the dynamics of wrinkle patterns, which may be exploited for surface patterning.

9.5 Wrinkle patterns under non-uniform stresses

For a thin film with finite lateral dimensions, the residual stress is typically non-uniform, due to stress relaxation along the edges [65-67]. As a result, the wrinkle pattern depends on the distribution of the residual stress in the film, which in turn depends on the shape and size of the film. Two potential applications may be envisaged here. First, one may observe the wrinkle patterns as a visual reflection of the residual stress, thus offering a measure of the underlying stress state. Second, one may design the film geometry to achieve desirable wrinkle patterns for functional applications, such as color control [25] and adhesion [14]. However, predicting the wrinkle patterns under non-uniform residual stresses is often challenging. The energy minimization approach is practically ineffective for this purpose. On the other hand, with slight modification, the kinetics approach has been employed to simulate wrinkle patterns under non-uniform stresses [34]. For simplicity, only isotropic elastic films are considered in this section.

First consider a long thin-film ribbon with a finite width b in the x direction ($-b/2 \le x \le b/2$), but infinite in the y direction. By a shear-lag model [34, 48], the residual stress in the ribbon is obtained as

$$\sigma_{xx}^R = -\sigma_0 \left[1 - \frac{\cosh(x/\lambda)}{\cosh(b/2\lambda)} \right], \tag{85}$$

$$\sigma_{yy}^R = -\sigma_0 \left[1 - \nu_f \frac{\cosh(x/\lambda)}{\cosh(b/2\lambda)} \right], \tag{86}$$

where σ_0 is the uniform stress magnitude before relaxation, assumed to be equi-biaxial compression, and $\lambda = \sqrt{\dfrac{\overline{E}_f H h}{\mu_R}}$ is the shear-lag length at the elastic limit of the substrate. The normalized shear-lag length (λ/h) is 1000 when $\mu_R/\overline{E}_f = 10^{-5}$ and $H/h = 10$. For a narrow ribbon, the stress in the width direction (σ_{xx}^R) is significantly relaxed over the entire ribbon, while the stress relaxation in the longitudinal direction (σ_{yy}^R) is relatively small, depending on the Poisson's ratio of the film. Thus, parallel wrinkles are expected to form for the narrow ribbon. As the ribbon width increases, the maximum stress in the x direction increases. Beyond a critical width, the maximum stress at the center of the ribbon ($x = 0$) becomes greater than the transition stress predicted by Eq. (84). Consequently, the parallel wrinkles become unstable at the center, where zigzag wrinkle patterns are expected to form. The critical ribbon width for this transition can be predicted by setting the maximum lateral stress equal to the transition stress [34]. Figure 19 shows the simulated wrinkle patterns in thin-film ribbons of different widths, by the kinetics approach using the non-uniform residual stresses given by Eqs. (85) and (86). For these simulations, the computational cell size is $5000h \times 5000h$, with a 512 by 512 grid. To simulate the free edges, the residual stress is set to be zero outside the ribbon area. As expected, the wrinkles remain uniaxial near the edges. For wide ribbons, the wrinkles become zigzag and disordered at the center. Only when the width of the ribbon is less than a critical value, parallel wrinkles are obtained over the entire ribbon. Similar wrinkle patterns has been observed experimentally [9, 20].
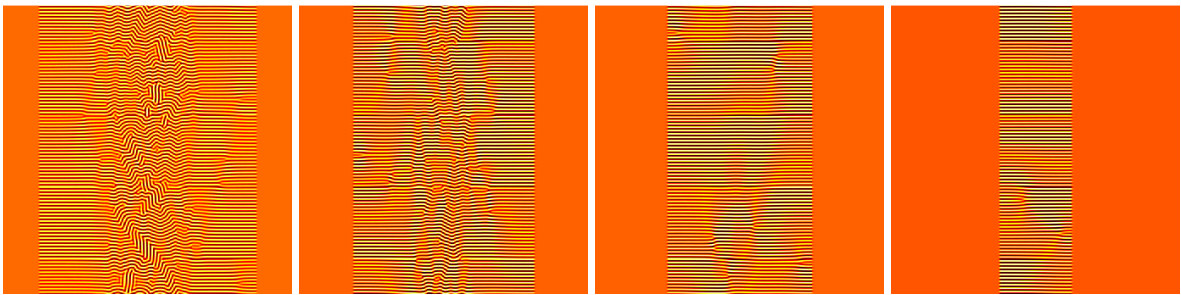

Figure 19. Simulated wrinkle patterns in thin-film ribbons. The ribbon widths are (from left to right): $b/h = 3750$, 3250, 2500, and 1250.

Next consider a rectangular thin film with widths b_x and b_y in the x and y directions, respectively. A two-dimensional (2D) shear-lag model may be used to determine the stress distribution in the rectangular film, which however can only be obtained numerically [68]. As an approximation, we extend the 1D solution in (85) and (86) to 2D as

$$\sigma_{xx}^R = -\sigma_0 \left[1 - \frac{\cosh(x/\lambda)}{\cosh(b_x/2\lambda)} \right] \left[1 - \nu_f \frac{\cosh(y/\lambda)}{\cosh(b_y/2\lambda)} \right], \tag{87}$$

$$\sigma_{yy}^R = -\sigma_0 \left[1 - \nu_f \frac{\cosh(x/\lambda)}{\cosh(b_x/2\lambda)} \right] \left[1 - \frac{\cosh(y/\lambda)}{\cosh(b_y/2\lambda)} \right]. \tag{88}$$

Using the approximate stress distribution, Figure 20 shows the simulated wrinkle patterns of a square film and two rectangular films [34]. For the square film ($b_x = b_y = 5000h$), parallel wrinkles develop near the mid-portion of the edges, while the four corners are wrinkle free due to stress relaxation in both directions; The center part of the film shows a fully developed labyrinth pattern. For the rectangular film with $b_x = 2500h$, predominantly parallel wrinkles extend from left to right except near the top and bottom edges where a small number of wrinkles in the perpendicular direction remain. With $b_x = 1250h$, only parallel wrinkles appear, with flat regions at the top and bottom. Choi et al. [9] observed similar wrinkle patterns in rectangular Si membranes bonded to a pre-strained PDMS. They also showed wrinkle patterns of other membrane geometries, including circles, ovals, hexagons, and triangles. For some applications, wrinkling may be undesirable. A wrinkle-free film may be achieved if the lateral dimensions are sufficiently small [44, 52, 66].
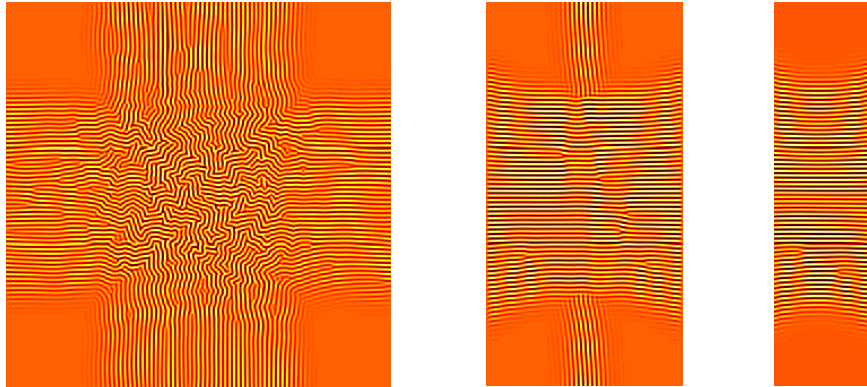

Figure 20. Simulated wrinkle patterns of a square film and two rectangular films, with $b_y/h = 5000$ and $b_x/h = 5000$, 2500, and 1250.
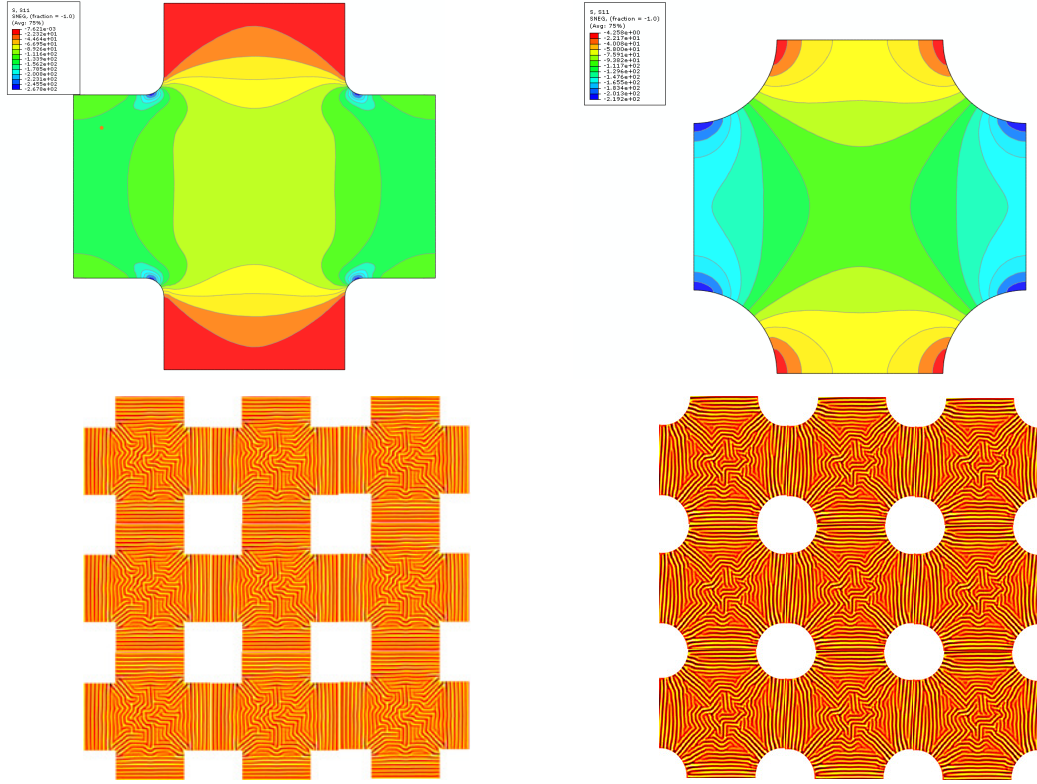
Figure 21. Wrinkling of periodically patterned films. Upper: distribution of residual stresses in a unit cell obtained from a finite element analysis. Lower: periodical replication of the wrinkle patterns.

To obtain ordered wrinkle patterns, Bowden et al. [10] fabricated bas-relief patterned surfaces and obtained a variety of wrinkle patterns with a thin metal film on an elastomer substrate. With the patterned surface, the residual stress in the metal film is likely non-uniform. However, the stress distribution is often complicated and cannot be predicted analytically. By the finite element method, the distribution of the residual stress in patterned thin films can be obtained numerically, assuming no wrinkles. Figure 21 shows the stress distributions for periodic patterns with square and circular holes [34]. The unit cell of each pattern is modeled as a two-dimensional plate on an elastic foundation, and the residual stress is calculated by invoking a mismatch in thermal expansion. Next, with the non-uniform stress distribution, evolution of wrinkle patterns is simulated by the kinetics approach [34]. To compare with the experimental observations, the resulting wrinkle patterns in the unit cell are replicated to produce the periodic wrinkles in a larger scale in Fig. 21, showing remarkably similar features as those reported by

Bowden et al. [10]. Therefore, it is possible to predict complex wrinkle patterns by combining the kinetics approach with the finite element method.

10. Concluding Remarks

In summary, a kinetics approach to wrinkling is presented in this chapter. It is demonstrated that the kinetics approach is capable of simulating evolution of wrinkle patterns under various conditions. Furthermore, it has enabled us to understand the dynamics of coarsening and pattern transition both analytically and numerically. The effects of stress anisotropy, material anisotropy, and non-uniform stress distribution on wrinkle patterns are elucidated by comparing numerical simulations with experimental observations.

Despite significant advances over the last decade in both theory and experiments, recent studies continue to show fascinating wrinkles that stimulate further studies. A few notable examples include concomitant wrinkling and delamination [69, 70], diffusion induced wrinkling [71, 72], and wrinkle patterns on curved surfaces [73, 74]. In addition to fundamental understanding, several recent reviews have highlighted potential applications of the wrinkling phenomena in stretchable electronics [75], metrology [76], adhesion [77], and micro/nano-fluidics [78].

References

1. Gough, G.S., Elam, C.F., De Bruyne, N.D., 1940. The stabilization of a thin sheet by a continuous supporting medium. J. Roy Aero. Soc. 44, 12-43.

2. Wan, C.C., 1947. Face buckling and core strength requirements in sandwich construction. J. Aero. Sci. 14, 531-539.

3. Goodier, J.N., and Neou, I.M., 1951. The evaluation of theoretical critical compression in sandwich plates. J. Aero. Sci. 18, 649-657.

4. Allen, H.G., 1969. *Analysis and Design of Structural Sandwich Panels*, Pergamon, New York.

5. Biot, M.A., 1957. Folding instability of a layered viscoelastic medium under compression. Proc. R. Soc. A 242, 444–454.

6. Biot, M.A., 1963. Surface instability of rubber in compression. Applied Scientific Research A 12, 168-182.

7. Watanabe, M., Shirai, H., Hirai, T., 2002. Wrinkled polypyrrole electrode for electroactive polymer actuators. J. Appl. Phys. 92 (8), 4631-4637.

8. Lacour, S.P., Wagner, S., Huang, Z.Y., Suo, Z., 2003. Stretchable gold conductors on elastomeric substrates. Appl. Phys. Lett. 82 (15), 2404-2406.

9. Choi, W.M., Song, J., Khang, D.-Y., Jiang, H., Huang, Y., Rogers, J.A., 2007. Biaxially stretchable "wavy" silicon nanomembranes. Nano Letters 7, 1655-1663.

10. Bowden, N., Brittain, S., Evans, A.G., Hutchinson, J.W., Whitesides, G.M., 1998. Spontaneous formation of ordered structures in thin films of metals supported on an elastomeric polymer. Nature 393, 146-149.

11. Ohzono, T., Shimomura, M., 2004. Ordering of microwrinkle patterns by compressive strain. Physical Review B 69, 132202.

12. Chan, E.P., and Crosby, A.J., 2006. Fabricating microlens arrays by surface wrinkling. Advanced Materials 18, 3238-3242.

13. Harrison, C., Stafford, C.M., Zhang, W., Karim, A., 2004. Sinusoidal phase grating created by a tunably buckled surface. Applied Physics Letters **85**, 4016-4018.

14. Chan, E.P., Smith, E.J., Hayward, R.C., Crosby, A.J., 2008. Surface wrinkles for smart adhesion. Advanced Materials 20, 711-716.

15. Stafford, C.M., Harrison, C., Beers, K.L., Karim, A., Amis, E.J., Vanlandingham, M.R., Kim, H.-C., Volksen, W., Miller, R.D., Simonyi, E.E., 2004. A buckling-based metrology for measuring the elastic moduli of polymeric thin films. Nature Materials **3**, 545-550.

16. C.M. Stafford, B.D. Vogt, C. Harrison, D. Julthongpiput, R. Huang, Elastic Moduli of Ultrathin Amorphous Polymer Films. Macromolecules 39, 5095-5099 (2006).

17. E.P. Chan, K.A. Page, S.H. Im, D.L. Patton, R. Huang, C.M. Stafford, Viscoelastic properties of confined polymer films measured via thermal wrinkling. Soft Matter 5, 4638-4641 (2009).

18. A.L. Volynskii, S. Bazhenov, O.V. Lebedeva, and N.F. Bakeev. Mechanical buckling instability of thin coatings deposited on soft polymer substrates. *Journal of Materials Science* 35(3):547-554, 2000.

19. P.J. Yoo and H.H. Lee. Evolution of a stress-driven pattern in thin bilayer films: Spinodal wrinkling. *Physical Review Letters* 91(15):154502-154502, 2003.

20. T. Okayasu, H.L. Zhang, D.G. Bucknall, G.A.D. Briggs, Spontaneous formation of ordered lateral patterns in polymer thin-film structures. Adv. Functional Materials 14, 1081-1088 (2004).

21. M. Kucken, A.C. Newell, A model for fingerprint formation. Europhysics Letters 68, 141-146 (2004).

22. K. Y. Volokh, Tissue morphogenesis: a surface buckling mechanism. Int. J. Dev. Biol. 50, 359-365 (2006).

23. C.C. Hilgetag and H. Barbas, Role of mechanical factors in the morphology of the primate cerebral cortex. PLoS Computational Biology 2, 146-159 (2006).

24. Sultan, E., Boudaoud, A., 2008. The buckling of a swollen thin gel layer bound to a compliant substrate. J. Appl. Mech. 75, 051002.

25. T. Xie, X. Xiao, J. Li, R. Wang, Encoding localized strain history through wrinkle based structural colors. Adv. Mater. 20, 4390-4394 (2010).

26. Tanaka, T., Sun, S.-T., Hirokawa, Y., Katayama, S., Kucera, J., Hirose, Y., Amiya, T., 1987. Mechanical instability of gels at the phase transition. Nature 325, 796-198.

27. Gent, A. N. and Cho, I. S., 1999. Surface instabilities in compressed or bent rubber blocks. Rubber Chemistry and Technology 72, 253-262.

28. Guvendiren, M., Yang, S., Burdick, J.A., 2009. Swelling-induced surface patterns in hydrogels with gradient crosslinking density. Advanced Functional Materials 19, 3038-3045.

29. M.K. Kang and R. Huang, Swell induced surface instability of confined hydrogel layers on substrates. J. Mech. Phys. Solids 58, 1582-1598 (2010).

30. R. Huang, Kinetic wrinkling of an elastic film on a viscoelastic substrate. Journal of the Mechanics and Physics of Solids 53, 63-89 (2005).

31. S.H. Im and R. Huang, Evolution of wrinkles in elastic-viscoelastic bilayer thin films. J. Applied Mechanics 72, 955-961 (2005).

32. R. Huang and S.H. Im, Dynamics of wrinkle growth and coarsening in stressed thin films. Physical Review E 74, 026214 (2006).

33. S. H. Im and R. Huang, Wrinkle Patterns of Anisotropic Crystal Films on Viscoelastic Substrates. J. Mech. Phys. Solids 56, 3315-3330 (2008).

34. S. H. Im, Wrinkling of elastic thin films on compliant substrates. PhD dissertation, University of Texas at Austin, 2009.

35. J. Groenewold. Wrinkling of plates coupled with soft elastic media. *Physica A* 298:32-45, 2001.

36. X. Chen and J.W. Hutchinson. Herringbone Buckling Patterns of Compressed Thin Films on Compliant Substrates. *Journal of Applied Mechanics* 71(5):597-603, 2004.

37. Z.Y. Huang, W. Hong, and Z. Suo. Nonlinear analyses of wrinkles in a film bonded to a compliant substrate. *Journal of the Mechanics & Physics of Solids* 53(9):2101-2118, 2005.

38. H. Jiang, D.Y. Khang, J. Song, Y. Sun, Y. Huang, and J.A. Rogers. Finite deformation mechanics in buckled thin films on compliant supports. *Proceedings of the National Academy of Sciences* 104(40):15607-15612, 2007.

39. J. Song, H. Jiang, W.M. Choi, D.Y. Khang, Y. Huang, and J.A. Rogers. An analytical study of two-dimensional buckling of thin films on compliant substrates. *Journal of Applied Physics* 103:014303, 2008.

40. B. Audoly and A. Boudaoud. Buckling of a stiff film bound to a compliant substrate Part I: Formulation, linear stability of cylindrical patterns, secondary bifurcations. *Journal of the Mechanics and Physics of Solids* 56(7):2401-2421, 2008.

41. N. Sridhar, D.J. Srolovitz, and Z. Suo. Kinetics of buckling of a compressed film on a viscous substrate. *Applied Physics Letters* 78(17):2482-2484, 2001.

42. R. Huang and Z. Suo. Wrinkling of a compressed elastic film on a viscous layer. *Journal of Applied Physics* 91(3):1135-1142, 2002.

43. R. Huang and Z. Suo. Instability of a compressed elastic film on a viscous layer. *International Journal of Solids and Structures* 39(7):1791-1802, 2002.

44. J. Liang, R. Huang, H. Yin, J. C. Sturm, K. D. Hobart, and Z. Suo, Relaxation of compressed elastic islands on a viscous layer. Acta Materialia 50, 2933-2944 (2002).

45. S. Timoshenko, *Theory of plates and shells*. McGraw-Hill, 1940.

46. L.D. Landau and E.M. Lifshitz. *Theory of elasticity*. Pergamon Press, 1959.

47. R.M. Christensen. *Theory of Viscoelasticity: An Introduction*. Academic Press, 1982.

48. Z.C. Xia and J.W. Hutchinson. Crack patterns in thin flms. *Journal of the Mechanics and Physics of Solids* 48:1107-1131, 2000.

49. R. Huang, J.H. Prevost, and Z. Suo, Loss of constraint on fracture in thin film structures due to creep. Acta Materialia 50, 4137-4148 (2002).

50. Z. Suo, J.H. Prévost, J. Liang, Kinetics of Crack Initiation and Growth in Organic-Containing Integrated Structures. *Journal of the Mechanics and Physics of Solids*, **51**, 2169-2190 (2003).

51. K.D. Hobart, F.J. Kub, M. Fatemi, M.E. Twigg, P.E. Thompson, T.S. Kuan, and C.K. Inoki. Compliant substrates: a comparative study of the relaxation mechanisms of strained films bonded to high and low viscosity oxides. *J. Electron. Mater* 29(7):897-900, 2000.

52. R.L. Peterson. Stretching Silicon: A uniaxial and biaxial strain generation process and the resulting mobility enhancement in silicon-on-insulator MOSFETs. Ph.D. dissertation, Princeton University, 2006.

53. L. Golubovic, D. Moldovan, and A. Peredera. Dynamics of the Euler Buckling Instability. *Physical Review Letters* 81:3387-3390, 1998.

54. D. Moldovan and L. Golubovic. Buckling Dynamics of Compressed Thin Sheets (Membranes). *Physical Review Letters* 82(14):2884-2887, 1999.

55. L. Sung, A. Karim, J.F. Douglas, and C.C. Han. Dimensional Crossover in the Phase Separation Kinetics of Thin Polymer Blend Films. *Physical Review Letters* 76(23):4368-4371, 1996.

56. W. Lu and Z. Suo. Dynamics of nanoscale pattern formation of an epitaxial monolayer. *Journal of the Mechanics and Physics of Solids* 49(9):1937-1950, 2001.

57. A.A. Golovin, S.H. Davis, and P.W. Voorhees. Self-organization of quantum dots in epitaxially strained solid films. *Physical Review E* 68(5):056203, 2003.

58. Y. Pang and R. Huang, Nonlinear effect of stress and wetting on surface evolution in epitaxial thin films. Physical Review B 74, 075413 (2006).

59. D. Breid, A.J. Crosby, Effect of stress state on wrinkle morphology. Soft Matter 7, 4490-4496 (2011).

60. S. Cai, D. Breid, A.J. Crosby, Z. Suo, J.W. Hutchinson, Periodic patterns and energy states of buckled films on compliant substrates. J. Mech. Phys. Solids 59, 1094-1114 (2011).

61. S.J. Kwon and H.H. Lee, Theoretical analysis of two-dimensional buckling patterns of thin metal-polymer bilayer on the substrate. J. Appl. Phys. 98, 063526 (2005).

62. T. Ohzono, M. Shimomura, Effect of thermal annealing and compression on the stability of microwrinkle patterns. Phys. Rev. E 72, 025203(R), 2005.

63. P.-C. Lin, S. Yang, Spontaneous formation of one-dimensional ripples in transit to highly ordered two-dimensional herringbone structures through sequential and unequal biaxial mechanical stretching. Appl. Phys. Lett. 90, 241903 (2007).

64. C.Y. Yu, P.W. Chen, S.R. Jan, M.H. Liao, K.-F. Liao, and C.W. Liu. Buckled SiGe layers by the oxidation of SiGe on viscous SiO_2 layers. *Applied Physics Letters* 86:011909 (2005).

65. T.W. Shield and K.S. Kim, Beam theory models for thin film segments cohesively bonded to an elastic half space. Int. J. Solids Struct. 29, 1085-1103 (1992).

66. H. Yin, R. Huang, K.D. Hobart, Z. Suo, T.S. Kuan, C.K. Inoki, S.R. Shieh, T.S. Duffy, F.J. Kub, J.C. Sturm, Strain relaxation of SiGe islands on compliant oxide. Journal of Applied Physics 91, 9716-9722 (2002).

67. L.B. Freund and S. Suresh, *Thin Film Materials: Stress, Defect Formation and Surface Evolution*. Cambridge University Press, 2003.

68. R. Huang, H. Yin, J. Liang, K. D. Hobart, J. C. Sturm, and Z. Suo, Relaxation of a strained elastic film on a viscous layer. MRS Symposium Proceedings, vol. 695, 115-120 (2001).

69. Mei, H., Huang, R., Chung, J.Y., Stafford, C.M., Yu, H.H., 2007. Buckling modes of elastic thin films on elastic substrates. Appl. Phys. Lett. 90, 151902.

70. Vella, D., Bico, J., Boudaoud, A., Roman, B., Reis, P.M., 2009. The macroscopic delamination of thin films from elastic substrates. PNAS 106, 10901-10906.

71. H. Vandeparre, P. Damman, Wrinkling of stimuloresponsive surfaces: mechanical instability coupled to diffusion. Phys. Rev. Lett. 101, 124301 (2008).

72. J.Y. Chung, A.J. Nolte, C.M. Stafford, Diffusion-controlled, self-organized growth of symmetric wrinkling patterns. Advanced Materials 21, 1358-1362 (2009).

73. X. Chen, J. Yin, Buckling patterns of thin films on curved compliant substrates with applications to morphogenesis and three-dimensional micro-fabrication. Soft Matter 6, 5667-5680 (2010).

74. B. Li, F. Jia, Y.-P. Cao, X.-Q. Feng, H. Gao, Surface wrinkling patterns on a core-shell soft sphere. Phys. Rev. Lett. 106, 234301 (2011).

75. D.-Y. Khang, J.A. Rogers, H.H. Lee, Mechanical buckling: mechanics, metrology, and stretchable electronics. Advanced Functional Materials 18, 1-11 (2008).

76. J.T. Chung, A.J. Nolte, C.M. Stafford, Surface wrinkling: a versatile platform for measuring thin-film properties. Advanced Materials 23, 349-368 (2011).

77. S. Yang, K. Khare, P.-C. Lin, Harnessing surface wrinkle patterns in soft matter. Advanced Functional Materials 20, 2550-2564 (2010).

78. Y. Mei, S. Kiravittaya, S. Harazim, O.G. Schmidt, Principles and applications of micro and nanoscale wrinkles. Materials Science and Engineering R 70, 209-224 (2010).